Chapter 11

Metal/Semiconductor Hybrid Nanocrystals and Synergistic Photocatalysis Applications

Jiatao Zhang, Muwei Ji, Jiajia Liu and Meng Xu

Additional information is available at the end of the chapter

http://dx.doi.org/10.5772/61888

Abstract

This review focuses on recent research efforts to synthesize metal/semiconductor hybrid nanocrystals, understand and control the photocatalytic applications. First, we summarize the synthesis methods and recent presented metal/seminconductor morphologies, including heterodimer, core/shell, and yolk/shell etc. The metal clusters and nanocrystals deposition on semiconductor micro/nano substrates with well-defined crystal face exposure will be clarified into heterodimer part. The outline of this synthesis part will be the large lattice mismatch directed interface, contact and morphologies evolution. For detailed instructions on each synthesis, the readers are referred to the corresponding literature. Secondly, the recent upcoming photocatalysis applications and research progress of these hybrid nanocrystals will be reviewed, including the photocatalytic hydrogen evolution (water splitting), photo-reduction of CO_2 and other newly emerging potential photosynthesis applications of metal/semiconductor hybrid nanocrystals. Finally, we summarize and outlook the future of this topic. From this review, we try to facilitate the understanding and further improvement of current and practical metal/semiconductor hybrid nanocrystals and photocatalysis applications.

Keywords: Metal/semiconductor, hybrid nanocrystals, photocatalysis, sythesis, interface, lattice mismatch, Plasmon, exciton, photooxidation, photoreduction

1. Introduction

The shape and size effect, the controllable doping, heterocomposite, and interface are the prerequisite of colloidal nanocrystals for exploring their optoelectronic properties, such as fluorescence, plasmon–exciton coupling, efficient electron/hole separation, and enhanced photoelectric conversion [1–4]. The use of photoexcited electrons and holes in semiconductor nanocrystals as reduction and oxidation reagents is an intriguing way of harvesting photon

energy to drive chemical reactions since increasing energy demand and environmental pollution create a pressing need for clean and sustainable energy solution. The high efficient separation and collection of photoexcited electrons (e-) and holes (h+) are the key points to get high efficient photocatalysis applications. Hybrid nanocrystals composed of semiconductor and metal components are receiving extensive attention in recent years due to their high efficient separation of photoexcited electrons and holes and potentional photocatalysis applications [1,4–5]. Furthermore, hybrid nanocrystals composed of semiconductor and plasmonic metal components are receiving extensive attention. The simultaneous existence and coupling of localized surface plasmon resonance induced plasmon and excitons in semiconductors, as well as the synergistic interactions between the two components [1, 6–7].

This review focuses on recent research efforts to synthesize metal/semiconductor hybrid nanocrystals to understand and control the photocatalytic applications. First, we summarize the synthesis methods and recent presented metal/semiconductor morphologies, including heterodimer, core/shell, and yolk/shell. The metal clusters and nanocrystals deposition on semiconductor micro/nanosubstrates with well-defined crystal face exposure will be clarified into heterodimer part. The outline of this synthesis part will be the large lattice mismatch-directed interface, contact, and morphology evolution. For detailed instructions on each synthesis, the readers are referred to the corresponding literature.

Second, the recent upcoming photocatalysis applications and research progress of these hybrid nanocrystals will be reviewed, including the photocatalytic hydrogen evolution (water splitting), photoreduction of CO_2, and other newly emerging potential photosynthesis applications of metal/semiconductor hybrid nanocrystals. Finally, we provide a summary and outlook on the future of this topic. From this review, we try to facilitate the understanding and further improvement of current and practical metal/semiconductor hybrid nanocrystals and photocatalysis applications.

2. Metal/semiconductor hybrid nanocrystal synthesis

According to the classical hetero epitaxial growth theory [8], when a secondary material (referred to as ''2'') has to be deposited over a preexisting seed substrate of a different material (denoted as ''1''), total Gibbs free surface energy change function ΔG_s can be described as follows: $\Delta G_s = \gamma_1 - \gamma_2 + \gamma_{1,2}$, where γ_1 and γ_2 are the surface energies of seed substrate and the deposited materials, respectively, the solid/solution interfacial energies of colloidal nanostructure in the liquid medium, and $\gamma_{1,2}$ is strain-related solid/solid interfacial energy that depends on the bonding strength and degree of crystallographic compatibility between materials 1 and 2. As shown in Figure 1, if material 2 exposes lower energy surfaces ($\gamma_2 < \gamma_1$) and/or attains good lattice matching with the material 1 ($\gamma_{1,2}$ is small), then it is easy to get continuous and uniform core/shell nanostructure ($\Delta G_s > 0$, Frank—van der Merwe (FM) growth mode). On the contrary, if material 2 is featured by higher energy surfaces ($\gamma_2 > \gamma_1$) and/or $\gamma_{1,2}$ is high owing to the large lattice mismatch, then it will tend to deposit as a discontinuous island-like

http://dx.doi.org/10.5772/61888

domain to be heterodimer structure (ΔG_s <0, Volmer—Weber (VW)growth mode) or even separate from each other. Therefore, the metal/semiconductor hybrid nanocrystal synthesis should follow the mechanism of Figure 1. However, in colloidal phase, γ_1 and γ_2 would be strongly influenced by adhesion of solvent, capping ligands and precursors, thus changing $\gamma_{1,2}$ too [9,10]. Considering of the significant impact of binding of organic stabilizers or other solution species to the surface energy terms and therefore altering the ultimate ΔG_s, the colloidal phase synthesis will be potential for the control of large lattice mismatch-directed shape evolution and morphology control when choosing different solvent, capping ligands, and reactant precursors.

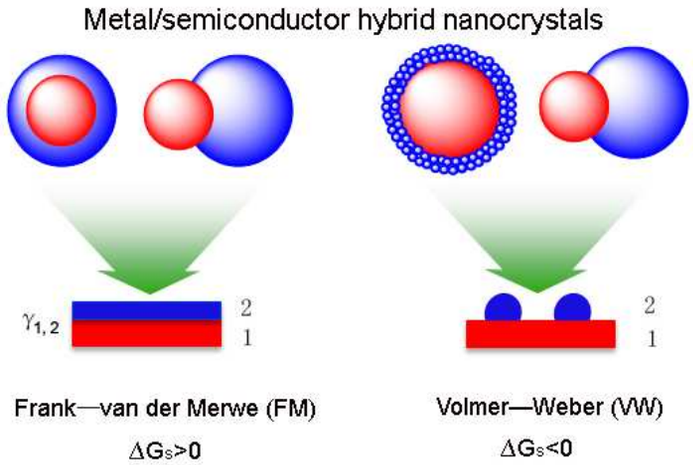

Figure 1. General metal/semiconductor hybrid nanocrystal synthesis sketches by traditional heterogeneous epitaxy growth mechanism: (A) Franck–van der Merwe (FM) mode; (B) Volmer–Weber (VM) mode.

2.1. Metal/semiconductor heterodimers by direct heterogeneous deposition

A broad family of metal/semiconductor hybrid nanocrystals has been obtained by accomplishing direct heterogeneous nucleation and growth of one or more secondary material layers onto preformed metal NC seeds serving as starting "cores" [9,10]. Synthetic strategies aim, on one side, at inhibiting homogeneous self-nucleation of isolated NCs made of the shell material and, on the other side, at achieving size- and shape-mediated deposition of the shell beyond limitations imposed by misfit strain at the metal/semiconductor interface. Practical techniques to realize these objectives rely on the colloidal synthesis, the "active" surface of "core" and the slow-nucleation of another material to deposit on "core" homogeneously, depending on the inherent chemical accessibility of the "core" or "seeds" as well on the reactivity of the shell molecular precursors (generally nonaqueous) solution media. The regulation of the thermodynamics and kinetics of reactions, namely, the temperature and selection of suitable surface-adhering organic ligands or surfactants and the optimal reactant injection rate all critically influence on the temporal evolution of the supersaturation degree.

To date, disparate combinations of metals, semiconductors, and oxides have been addressed by manipulating direct heterogeneous deposition pathways [11–25]. Here, we typically review most recent achievement in the field, the metal/semiconductor heterodimers (as scheme in Figure 1). Representative transmission electron microscopy (TEM) and high-resolution TEM examples of core–shell NCs can be found in Figure 2, respectively.

The one-pot synthesis of metal/semiconductor heterodimers mostly focus on the bifunctional heterodimers of nanoparticles, such as the conjugate of quantum dots (QDs) and magnetic nanoparticles reported by Gu et al. [20], the noble metal/metal oxide heterodimers by Wang et al. [21] and Wu et al. [22], and the bimagnetic FePt–iron oxide heterodimer nanocrystals by Figuerola et al. [23] and Cozzoli et al. [24] (see also Figure 2).

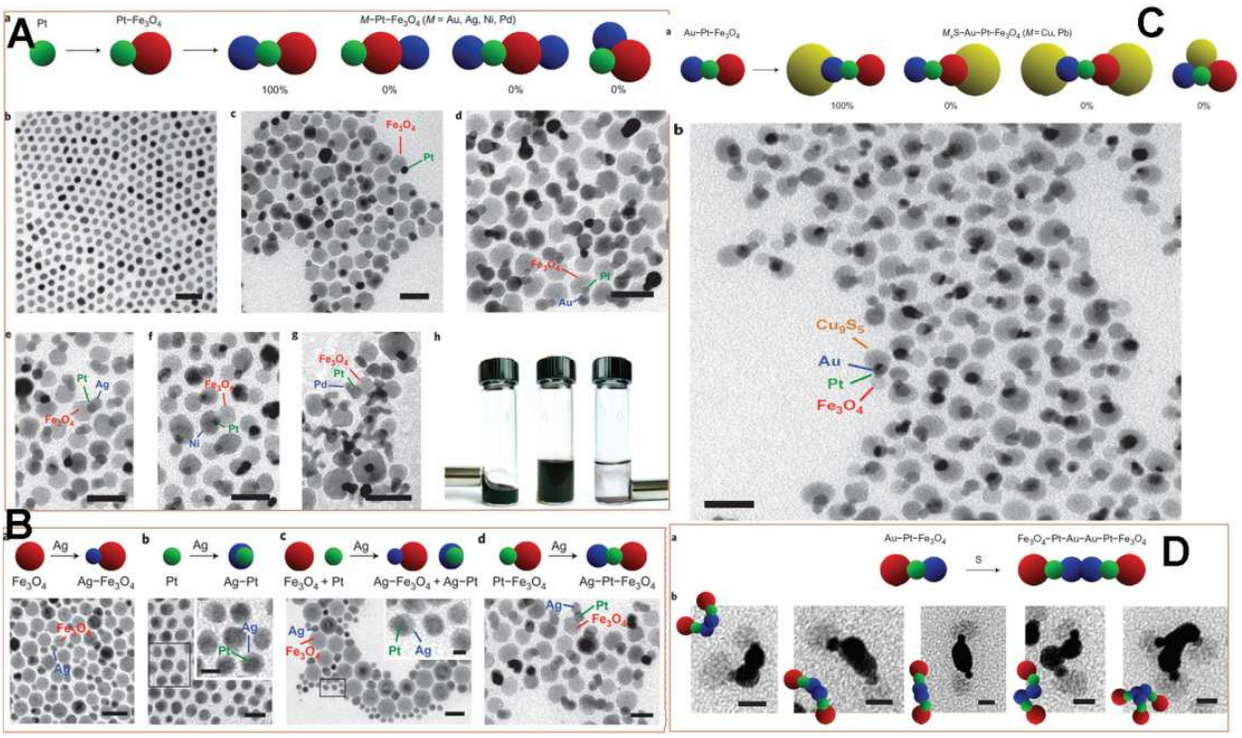

Figure 2. (A) FePt/CdS heterodimers by one-pot synthesis: (a) the scheme of synthesis process, (b) a TEM image, and (c) a high-resolution TEM image of FePt/CdS heterodimers. Adapted from Gu et al. [20] with permission; copyright American Chemical Society. (B) Seed-mediated high temperature growth of M/metal oxide heterodimers: (a) the scheme of synthesis, (b) 5–12 nm Au–Fe_3O_4, (c) 5–12 nm Ag-Fe_3O_4, and (d) 5–12 nm Pt–Fe_3O_4. Adapted from Wang et al. [21] with permission; copyright American Chemical Society. FePt/In_2O_3 heterodimers were adapted from Wu et al. [22] with permission; copyright American Chemical Society. (C) One-pot, two-step colloidal strategy to prepare FePt/ iron oxide heterodimer nanocrystals: (a) the scheme of synthesis method; (b) the TEM image of FePt/ Iron Oxide heterodimers; and (c) the HRTEM image of FePt/ Iron Oxide heterodimer. Adapted from Figuerola et al. [23] and Cozzoli et al. [24] with permission; copyright American Chemical Society.

The Au/ CdSe or Au/CdS heterodimer nanocrystals, because of the noble metal and II-VI QDs, are potential for photocatalysis applications. Banin et al. used surface nucleation and growth of a second phase to get Au/CdSe nanorod (NR) heterodimers, the first time to realize site-selective growth of Au NPs on CdSe NRs tips (see also Figure 3A) [13, 25, 26]. Du et al. used

http://dx.doi.org/10.5772/61888

similar way to directly deposit the Au NPs on CdS NRs to get heterodimers (see also Figure 3B) [27]. The as-obtained Au/CdS and Au/CdSe NR heterodimers promote the electron/hole separation and exhibit promising photocatalytic activity for the water-splitting reaction in photoelectrochemical cells and photodegradation applications.

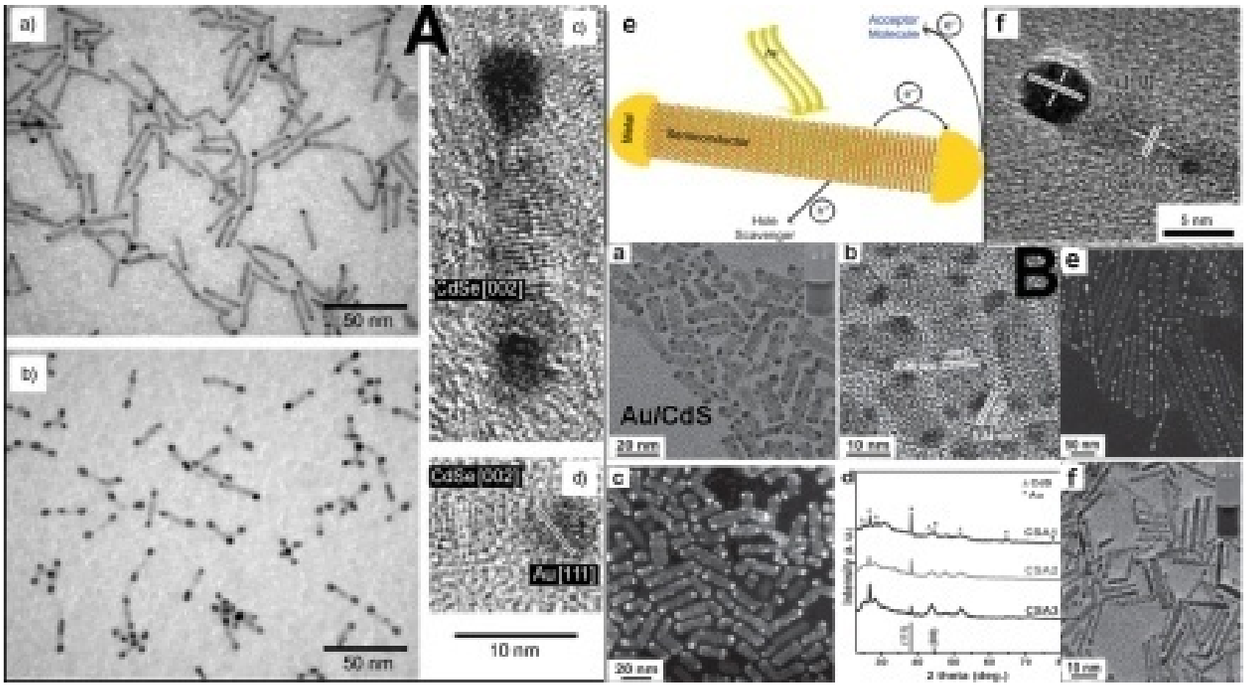

Figure 3. (A) TEM images showing controlled growth of gold onto the tips of CdSe nanorods. (a, b) The size of the gold tips can be controlled by varying the amount of gold precursor added during growth. (c, d) HRTEM images of a single nanodumbbell (c) and a nanodumbbell tip (d); the CdSe lattice for the rod in the center and gold tips at the rod edges can be identified. (From [25, 26], reprinted with permission from the AAAS.) (B) (a) TEM image, (b) HRTEM image, and (c) HAADF-STEM image of Au/CdS NRs hybrid nanocrystals. (d) XRD patterns of hybrid nanocrystals of Au/CdS NRs. (e) HAADF-STEM images in which the size of Au NPs is ~8 nm. (f) TEM images of Au/CdS hybrid nanocrystals in which the size of Au NPs is ~3 nm. Adapted from Du et al. [27] with permission; copyright Wiley-VCH Verlag GmbH & Co. KGaA.

Colloidal metal/semiconductor hybrid nanoparticles contain multiple nanoscale domains fused together by solid-state interfaces. They represent an emerging class of multifunctional lab-on-a-particle architectures that underpin future advances in solar energy conversion, photocatalysis. Buck et al. reported that the known direct heterogeneous deposition could be applied in a predictable and stepwise manner to build complex hybrid nanoparticle architectures that include M–Pt–Fe_3O_4 (M=Au, Ag, Ni, Pd) heterotrimers, M_xS–Au–Pt–Fe_3O_4 (M=Pb, Cu) heterotetramers, and higher-order oligomers based on the heterotrimeric Au–Pt–Fe_3O_4 building block [18]. This synthetic framework conceptually mimics the total synthesis approach used by chemists to construct complex organic molecules (see Figure 4).

In other words, the advantage of direct heterogeneous deposition colloidal method is it could get heterodimers with high monodispersity. The disadvantages are as follows: (1) The metal part or semiconductor part could not be mediated in more larger size range, such as tens of nanometers to hundreds of nanometers due to the Lar Mer growth mechanism of high

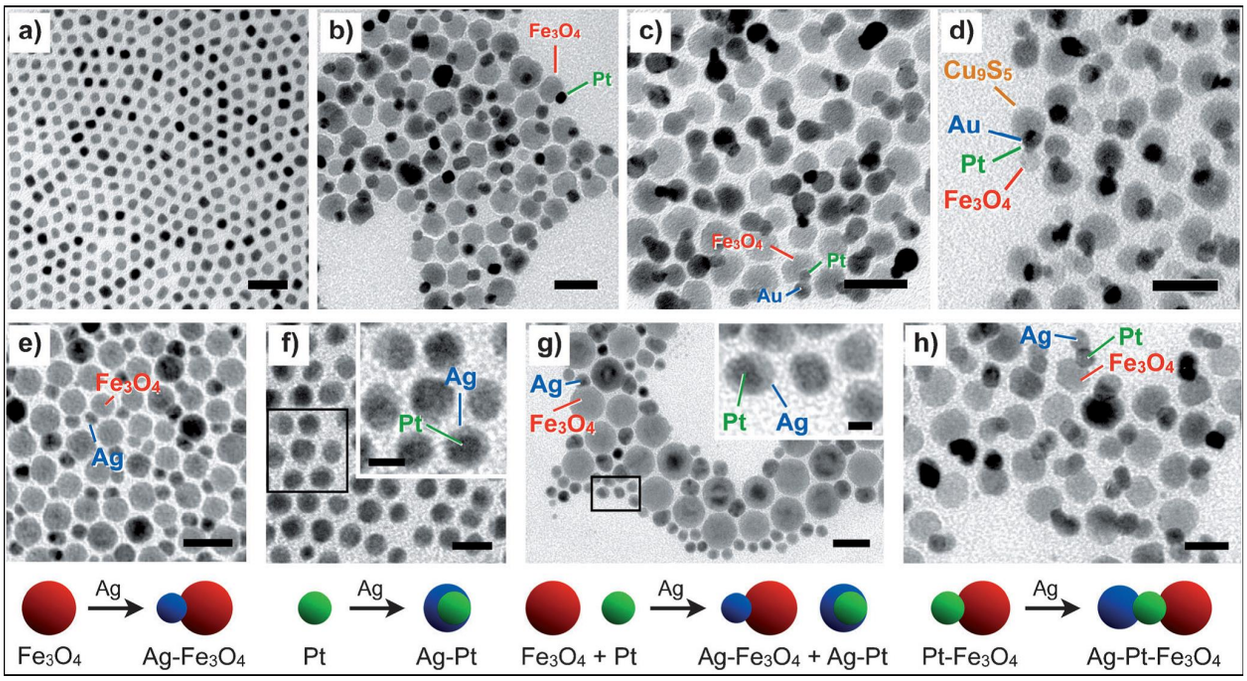

Figure 4. (A–D) TEM images showing the stepwise direct heterogeneous deposition of linear nanoparticle heterotetramers: (A) Pt nanoparticles, (B) Pt–Fe_3O_4 heterodimers, (C) Au–Pt–Fe_3O_4 heterotrimers, and (D) Cu_9S_5–Au–Pt–Fe_3O_4 heterotetramers. (E–H) TEM images and schematic representations showing a series of metal/semiconductor heterodimers (same synthetic conditions for all steps) aimed at understanding the site-selective deposition of Ag onto Pt–Fe_3O_4 heterodimers: (E) Ag grown off Fe_3O_4 nanoparticles, (F) Ag grown off Pt nanoparticles, (G) Ag grown indiscriminately off both Fe_3O_4 and Pt nanoparticles when both are present as a physical mixture, and (H) Ag grown exclusively off the Pt domain when Pt and Fe_3O_4 are directly attached as heterodimers. Reprinted from Buck et al. [18] with permission (Copyright of Nature group 2011, Macmillan Publishers Limited).

temperature organic phase synthesis. (2) The interface between metal and semiconductor is still not controlled well to be clear enough because of the size of two parts mostly still limited at <10 nm range. The lattice mismatch-induced stain energy here is usually too large to get more defects on the interface, which is not helpful for the highly efficient photoinduced electron/hole separation and the following photocatalysis applications.

2.2. Large lattice mismatch-directed shape evolution and morphology control

The growth of monocrystalline semiconductor-based metal/semiconductor hybrid nanostructures with modulated composition, morphology, and interface strain are the prerequisite for exploring their plasmon–exciton coupling, efficient electron/hole separation, and enhanced photocatalysis properties. As the schematic process in Figure 1, different from generally used one-pot epitaxial growth on performed metal nanoparticle seeds, Ouyang et al. and Zhang et al. unprecedentedly took two steps of facile chemical thermodynamics processes to maximally adjust the surface energies γ_2, $\gamma_{1,2}$, and then ΔG_s to change their overgrowth modes from FM mode to VW mode gradually. Furthermore, Ouyang et al. and Zhang et al. unprecedentedly used the cation exchange initiated the topotactic in situ conversion from amorphous to be single-crystalline structure [28–33]. In this case, the more flexible size range (from smaller than

http://dx.doi.org/10.5772/61888

10 nm to tens of nanometers, to hundreds of nanometers, and to micrometer scale), morphology (isotropic and anisotropic), interface, and single-crystallinity of metal and semiconductor part could be tailored synergistically.

By controlling soft acid–base coordination reactions between molecular complexes and colloidal nanostructures, Zhang et al. and Ouyang et al. showed that chemical thermodynamics could drive nanoscale monocrystalline growth of the semiconductor shell on metal nanosubstrates and then enhanced light–matter-spin interactions in these judiciously engineered nanostructures could be achieved [28, 3].

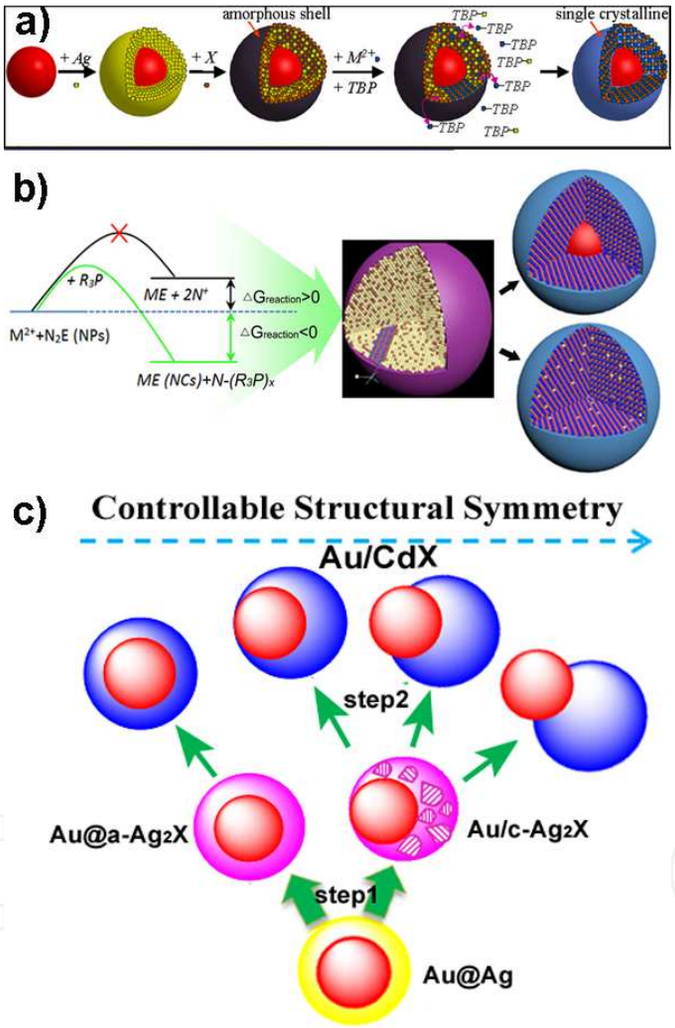

Figure 5. Schemes of large lattice mismatch-directed shape evolution and morphology control by Ouyang et al. and Zhang et al.: (A) Nonepitaxial growth process and mechanism of hybrid core–shell nanostructures with substantial lattice mismatches. From Zhang et al. [28], reprinted with permission from the AAAS. (B) The cation exchange reaction initiated by different phosphines or phosphites (R3P) and phosphine-initiated cation exchange for precisely tailoring composition and properties of metal/semiconductor nanostructures. (C) The schematic process of controllable structural symmetries in Au/CdX (X = S, Se, and Te) hybrid structures with large lattice mismatch by two steps of in situ chemical conversion. The a-Ag_2X means amorphous Ag_2X, c-Ag_2X means crystalline Ag_2X. Adapted from Gui et al. [31] and Zhao et al. [32] with permission; copyright Wiley-VCH Verlag GmbH & Co. KGaA.

First, as shown in Figure 5A, based on the Lewis acid–base reaction mechanism, where the entire nanostructure is spatially confined by an amorphous matrix, the monocrystalline growth of the semiconductor shell is fully directed by chemical thermodynamic properties of reactions within the matrix; the shell's lattice structure can be independent of that of the core NPs, thus circumventing the limitations imposed by epitaxial strategies. Starting from the core NPs, an overlayer of metal with soft Lewis acidity is grown onto the core. For all hybrid core–shell structures, we choose an Ag metal overlayer. The silver shells can be modified to form silver compound shells (Ag_2X) with an amorphous structure, providing a crucial platform for the next chemical transformation stage, ultimately leading to monocrystalline growth. It has been demonstrated that nanoscale chemical transformations, such as cation exchange, represent a versatile route for converting one crystalline solid to another [34, 35]. They show that this process can be harnessed to drive the single-crystal growth by carefully controlling the thermodynamic properties of reaction (1).

Tributylphosphine (TBP) was selected because it is a soft base and can behave as a phase-transfer agent to transport metal ions (Mn^+) to the surface of the core NPs by binding to free cations in solution. The high acid softness of Ag^+ favors the exchange process between Ag^+ in the amorphous matrix and Mn^+ in solution as long as the softness of Mn^+ is small enough to result in a positive ΔG.

Second, based on above research achievements, as shown in Figure 5B, Zhang et al. further studied the cation exchange reaction here. It has been explored that different phosphines could modulate the thermodynamic and kinetic parameters of the cation exchange reaction to synthesize complex semiconductor nanostructures [31]. Here, we take the examples of cation exchange between N^+ in amorphous N_2E (E means chalcogen) nanoparticles (NPs) and M^{2+} (such as Cd^{2+}) ions in solution, as shown in reaction (2) and Figure 1. Besides TBP, many other phosphine choices have been studied to mediate the thermodynamics and kinetics of reaction (2). Initiated by trace phosphine (R3P), the crystallization, the morphology, and the composition of metal/ME core/shell NCs have been tailored well.

The thermodynamics and kinetics of different phosphine and phosphite agents to synthesize semiconductor shell have been studied. The prerequisite to forward the cation exchange is the lone-pair electrons of P atom in phosphines or phosphites. Based on this, different π-accepting and σ-donating capabilities of them to M and N ions make reaction (2) to be exothermic (ΔG reaction < 0). Different phosphine coordinating to Ag^+ and Cd^{2+} and their coordination abilities study further prove reaction (2) is exothermic in principle. Therefore, thermodynamics and kinetics of reaction (2) could be mediated. The stronger coordination ability of R3P to N^+ than to M^{2+} ions enables in situ conversion of amorphous N_2E nanoparticles to be ME NCs. Although many kinds of phosphine or phosphite are applicable in reaction (2) thermodynamically, the steric effect derived from carbonyl ligands, such as alkyl and aryl ligands, would influence the kinetics of reaction (2), and the crystallization and composition of produced ME NCs distinctly. They took the example of cation exchange from amorphous Ag_2S nanostructure to single-crystalline CdS nanostructure. The kinetic activity order here is $PEt_3 > P(MeO)_3 > P(EtO)_3 > P(n\text{-}Bu)_3 > PPh_3 > P(n\text{-}Oct)_3 > P(PhMe)_3 > P(PhOMe)_3$. This is almost consistent with their σ donation ability order and contrary to their π back-bonding order. In particular, the steric hindrance

from carbonyl ligands would influence σ donation ability and then chemical kinetics distinctly. That is the reason why $P(PhOMe)_3$ phosphines have low activities to reaction (2). These findings are concordant with Chad Tolman's classic phosphine ligands ordering in terms of their electron-donating ability and steric bulk. Besides preserving the original shape and size, phosphine-initiated cation exchange reactions show potential to precisely tune the crystallinity and composition of metal/semiconductor hybrid nanocrystals.

Third, as illustrated in Figure 5C, Zhang et al. further showed that the structural symmetry of such metal/semiconductor hybrid heterostructures can be finely tuned with controllable separation between metal and semiconductor components by taking advantage of chemical thermodynamics-directed colloidal strain tuning, from symmetric core–shell to asymmetric heterodimer gradually by in situ conversion of amorphous/crystalline Ag_2X shell to be single crystalline CdX. Typically, nanoparticle/solution interfacial energies and heterointerfacial energy (due to the lattice mismatch) can be strongly influenced by adhesion of solvent, capping ligands and precursors in colloidal phase [9]. Here, Zhang et al. took a facile two-step approach to maximize these effects to precisely control gradual shape evolution from symmetric core/shell to asymmetric heterodimer nanostructures, as shown in Figure 5C [32]. This approach is fundamentally different from generally used one-pot epitaxial overgrowth with metal nanoparticle seeds [11-25]. First, they started with concentric Au–Ag core/shell. The fact of close lattice feature between Au and Ag makes it possible to achieve precise control of core size, shell thickness, and monodispersity based on Frank-van der Merwe growth mode [9]. Moreover, the higher reactivity of silver metal nanostructures than gold enables the in situ conversion of Ag shell to silver chalcogenide (Ag_2X) without modification of the Au metal core. Depending on reaction condition (such as temperature and reactants), the crystallinity of Ag_2X can be controlled from amorphous to partial crystalline, thus leading to different lattice mismatch between Au core and Ag_2X shell. As a result, different interfacial lattice strain between Au and Ag_2X can be induced to initiate phase separation to a certain extent. Different from the long time aging-induced elemental Au diffusion in Au–Ag_2X core/shell nanocrystals via Ostwald ripening, the Au–Ag_2X here was used as intermediate precursor to carry out next step quickly to get Au/CdX heteronanocrystals. Second, they utilized cation exchange process based on the theory of hard-soft acid and base to realize the in situ conversion of Ag_2X to monocrystalline CdX [28]. The cation exchange-induced cation rearrangement and crystallography texture transformation provide further impetus to shift CdX shell gradually because of the larger strain energy between Au and monocrystalline CdX. In general, the higher crystallization of Ag_2X shell as well as the higher reaction temperature of cation exchange reaction leads to larger phase separation between Au and CdX to reduce interfacial and grain boundary energies. These tunable relocations of gold to CdX in quantum size region would enable maximum degree of tunability of their optoelectronic properties coupling.

2.3. Metal/semiconductor core/shell nanocrystals

The growth of single-crystal semiconductor-based heterostructures with modulated composition is a prerequisite for exploring fundamental nanoscale semiconductor physics [36] and can offer technological devices with optimum characteristics, including enhanced

optical properties with high quantum yields [37], engineered electronic band gaps [38–40], and various solid-state optoelectronic properties [41–43]. Unintentional crystalline imperfections (such as polycrystallinity, dislocations, and other structural defects) lead to performance degradation or even premature failure of devices. For example, although the optical quality of semiconductor CdSe nanoparticles (NPs) could be improved by an overlayer of epitaxially grown CdS or ZnS, problems appear once the shell thickness becomes larger than the critical layer thickness (about two monolayers) due to the existence of strain-induced defects [38, 44, 45].

Current methods that achieve high-quality monocrystalline heterostructures are all based on epitaxial growth, as shown in Figure 1, which requires moderate lattice mismatches (<2%) between the two different materials. This lattice-matching constraint is a severe obstacle, particularly for growth of core–shell nanostructures with (quasi)spherical core NPs with highly curved surfaces that present many different crystallographic facets [46]. In addition to such lattice-matching requirements, the issues related to differences in crystal structure, bonding, and other properties have been found to inhibit epitaxial growth of dissimilar hybrid materials such as monocrystalline semiconductors on metals [47]. Attempts to use epitaxy to achieve hybrid metal core–semiconductor shell nanostructures have been unsuccessful, resulting in either polycrystalline semiconductor shells or anisotropic structures with segregation of the core and shell. This is only because as Figure 1 schemed, under large lattice mismatch (>40%), the semiconductor nanostructures would grow as small island-shaped NPs on metal core surface to decrease the surface strain energy. In this case, the Volmer—Weber (VW) mode growth would happen. Thus, based on these direct heterogeneous deposition methods, such as Figures 2–4 demonstrated, the polycrystalline semiconductor shell formed finally. As Figure 6 demonstrated, the Klimov, Talapin, and Wang groups have tried these kinds of method to prepare Au–PbS, Co–CdSe, Au–CdS, and Au–ZnS core/shell hybrid nanocrystals. Although they are highly monodispersed and could self-assemble into superlattice, the polycrystalline shell and too many defects at the interface limited their usefulness, especially in photocatalysis applications [48–53].

The photocatalysis application in the integration of semiconductor nanocrystals with noble metals uses the localized surface plasmon resonance (LSPR) effect of the metal component to enhance the light absorption, charge separation, and facilitate the absorbed light energy transfer from the metal to the semiconductor component for technologically important light-involved applications. Abundant studies have been devoted to the controllable productions of various hybrid nanocrystals. Heterostructure preparation is the basis for any application of semiconductor/noble metal hybrid nanocrystals. The crystalline imperfections of each component and the defects on the interface lead to the performance degradation or lost. Currently, high-quality monocrystalline heterostructures are usually produced by thermal decomposition epitaxial growth or through cation-exchange processes. The reported studies of monocrystalline hybrid nanocrystal synthesis are mainly based on epitaxial growth, which requires a moderate lattice mismatches between the different components. The lattice-mismatching constraint seriously limits the application of this method, particularly for growth of core/shell hybrid nanocrystals with highly curved surfaces. Therefore, it is a great challenge to synthesize the large lattice-mismatching semiconductor/metal hybrid nanocrystals with monocrystalline compounds and clear interface. Cation exchange reaction is a successful

http://dx.doi.org/10.5772/61888

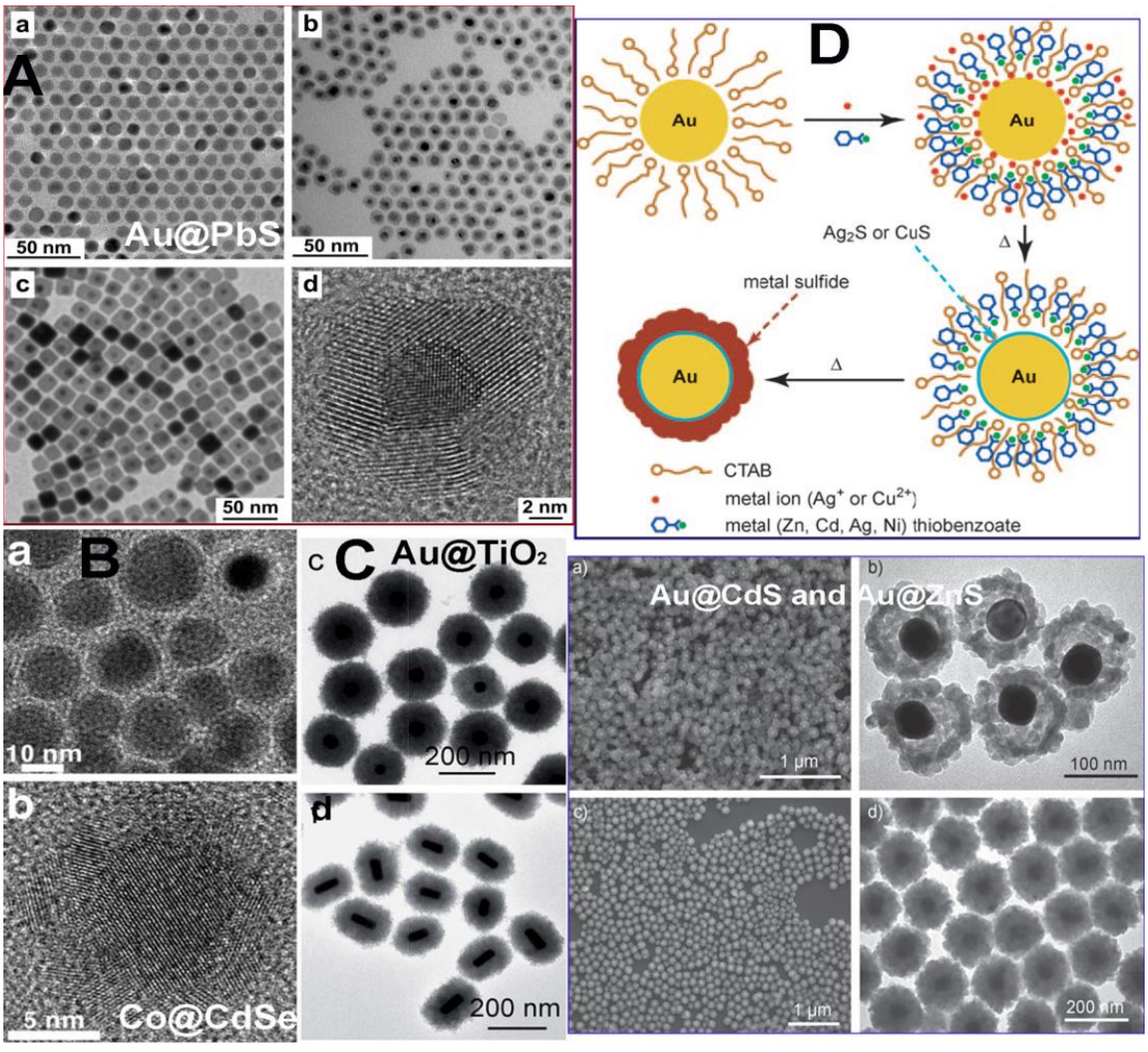

Figure 6. The metal/semiconductor core/shell NCs with polycrystalline semiconductor shell by direct heterogeneous deposition method. (A) Au–PbS core/shell NCs. (B) Co–CdSe core/shell NCs. Adapted from Lee et al. [48] and Kim et al. [49], respectively, with permission; copyright American Chemical Society. (C) Au–TiO_2 core/shell NCs. Adapted from Fang et al. [53] with permission; copyright Royal Society of Chemistry. (D) Au–CdS and Au–ZnS core/shell NCs. Adapted from Sun et al. [54] with permission; copyright Wiley-VCH Verlag GmbH & Co. KGaA.

synthetic method to preparation hybrid large lattice-mismatching heterodimer and core/shell nanocrystals with monocrystalline compounds and clear interface, which cannot be obtained by conventional epitaxial techniques [48–54]. Based on the Lewis acid–base reaction between molecular complexes and colloidal nanocrystals, the amorphous nanostructures can be transferred into monocrystalline compounds. Hence, by combining the sulfidation, selenization, or hyperoxidation of silver with cation exchange, other monocrystalline metal chalcogenide, selenide, or oxide nanostructures can been nonepitaxially grown on the large lattice-mismatching metal surface [28–33]. For the catalytic applications of semiconductor/noble metal hybrid nanocrystals, the key challenges are to obtain a clear semiconductor–metal interface and precise control over the size and shape of the heterostructures. Via cation exchange reaction, a series of semiconductor/metal hybrid nanocrystals can be obtained from concentric core–shell to nonconcentric heterodimer with precisely controlled separation and

clear interface between the semiconductor and noble metal compounds. The symmetry evolution of semiconductor/metal hybrid nanocrystal has led to novel control of light absorption and photocatalytic activity, which indicates the advantage of cation exchange nonepitaxial growth and the importance of nanoscale interface control. For the phosphine-initiated cation exchange, different phosphines have been used to modulate the thermodynamic and kinetic process of the cation exchange reaction in semiconductor nanocrystal synthesis. By using different phosphines, the crystallinity, composition, morphology, and related properties of semiconductors can be precisely controlled.

Different from the reports in Figure 6, Ouyang et al. and Zhang et al. used the nonepitaxial growth scheme (Figure 5A) to get metal–semiconductor core/shell NCs with single crystalline semiconductor shell. The size of metal, semiconductor shell, and the composition of semiconductor shell could be precisely controlled (Figures 7–9) [28].

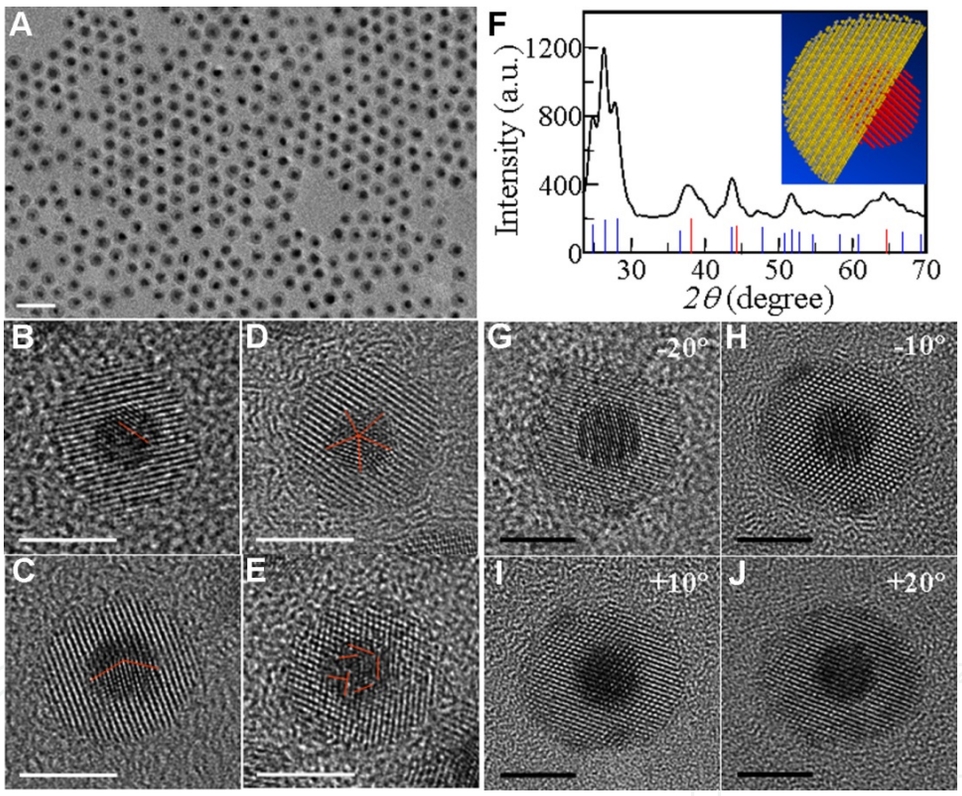

Figure 7. Au–CdS core–shell nanostructures with monocrystalline shell. (A) Typical TEM image showing uniform core–shell nanostructures. Scale bar, 20 nm. (B–E) High-resolution TEM images of core–shell nanostructures from (A). Whereas Au core NPs can manifest monocrystalline (B), single-fold twin (C), fivefold twin (D), and multiple-twin (E) lattice structures, all CdS shells are monocrystalline. The red lines highlight the lattice orientations within the Au core NPs. Scale bar, 5 nm. (F) XRD pattern of Au–CdS sample shown in panel A. Bulk Au [red solid lines, Joint Committee on Powder Diffraction Standards (JCPDS) #04-0784] and wurtzite CdS (blue solid lines, JCPDS #41-1049) are also provided for reference and comparison. (Inset) A ball-and-stick molecular model of Au–CdS, illustrating a cubic core and wurtzite shell. (G–J) Angle-dependent high-resolution TEM characterization. The sample depicted has a larger shell thickness than the one in panel A to emphasize the extremely high-quality crystallinity of the shell. The CdS shell shows perfect monocrystalline features without detectable structural defects under a different viewing angle. Scale bar, 5 nm. From Zhang et al. [28], reprinted with permission from the AAAS.

http://dx.doi.org/10.5772/61888

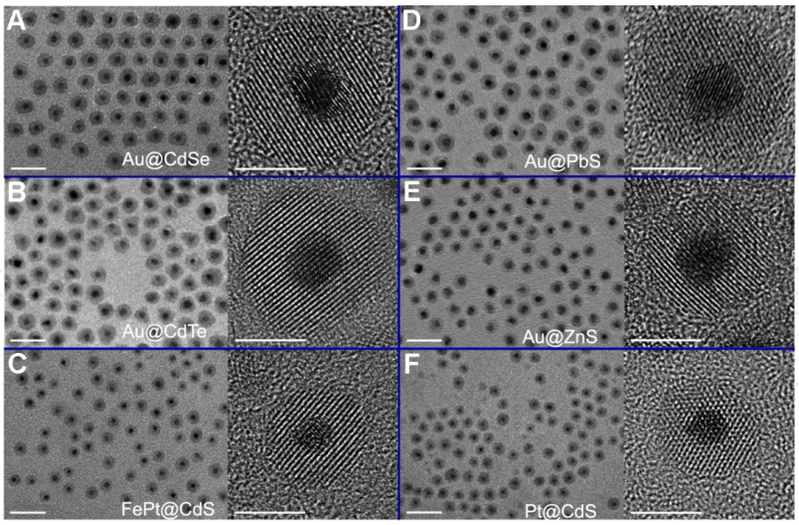

Figure 8. Large-scale (left) and high-resolution (right) TEM images of different hybrid core–shell nanostructures with various combinations of the core and shell components. All semiconductor shells show monocrystalline features. Scale bars for large-scale and high-resolution TEM images are 20 and 5 nm, respectively. (A) Au–CdSe; (B) Au–CdTe; (C) FePt–CdS; (D) Au–PbS; (E) Au–ZnS; and (F) Pt–CdS. From Zhang et al. [28], reprinted with permission from the AAAS.

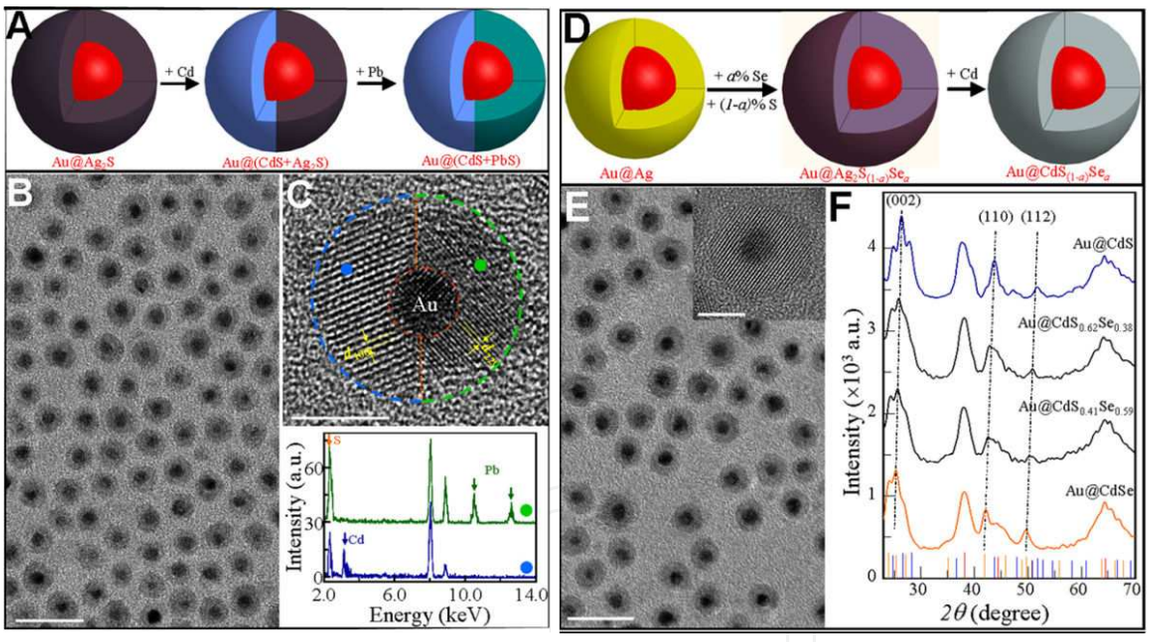

Figure 9. Growth of complex hybrid core–shell nanostructures with tailored structures and compositions of the monocrystalline shells. (A–C) Control of the monocrystalline cation species within the shell: the case of Au–(CdS+PbS). (A) Schematic of the growth procedure. (B) Large-scale TEM image. Scale bar, 20 nm. (C) (Top) High-resolution TEM image. Blue and green dashed arc curves highlight the monocrystalline CdS and PbS regimes, respectively. CdS and PbS manifest distinct lattice planes that can be assigned to (100) and (220), respectively. Scale bar, 5 nm. (Bottom) Single-particle EDS measurements in the CdS and PbS regimes. Peaks from Cd, Pb, and S elements are highlighted. (D–F) Control of the monocrystalline anion species within the shell: the case of Au–CdS1–aSea. (D) Schematic growth procedure. (E) Large-scale TEM image. Scale bar, 20 nm. (Inset) High-resolution TEM image showing the monocrystalline alloy shell. Scale bar, 5 nm. (F) XRD patterns highlighting lattice evolution from CdSe to CdS with different ratio a. From Zhang et al. [28], reprinted with permission from the AAAS.

Based on the strategy in Figure 5B, Zhang et al. use air-stable PPh_3 for the first time to initiate cation exchange reaction (2). Figure 10 demonstrates the Au–CdS, Pt–CdS core/shell NCs preparation by PPh_3 initiated reaction (2). Following the nonepitaxial growth process we published before [28] after cation exchange from amorphous Ag_2S shell, Au–CdS and Pt–CdS NCs could preserve thick monocrystalline CdS shell. LRTEM and HRTEM images in Figure 10A–D confirmed their good crystallization. Especially, as shown in Figure 10D, despite of anisotropic shape of Pt nanocube, the thick CdS shell has good single-crystallinity. PPh_3 further facilitates the monocrystalline engineering to break through critical layer thickness limit of heteroepitaxy. PPh_3 is "green" choice than TBP because it is air-stable enough to enable reaction (2) under more flexibly conditions, such as higher temperature and longer time to facilitate versatile ME NCs crystallization. Moreover, besides crystallization tailoring, PPh_3 could initiate cation exchange to get more complex heterostructures with precise compositional tailoring. Figure 11A and B showed the LRTEM and HRTEM images of as-prepared Au–$CdS_{1-x}Se_x$ core/shell nanocrystals with ternary single-crystal alloys shell. The S-to-Se ratio could be tailored ($CdS_{0.58}Se_{0.42}$ and $CdS_{0.45}Se_{0.55}$, obtained by EDS elemental analysis) to engineer their band gaps. The consistent shift of their powder XRD peaks from $CdS_{1-x}Se_x$ shell (Figure 11C) and the distinct colloid color changing (insert in Figure 3D) confirmed the homogeneous composition modulation. The strong visible light absorption (550–700 nm) (Figure 11D) due to the surface plasmon resonance (SPR) and exciton coupling in as-prepared Au–$CdS_{1-x}Se_x$ NCs indicated their potential photocatalysis and photovoltaic applications [55].

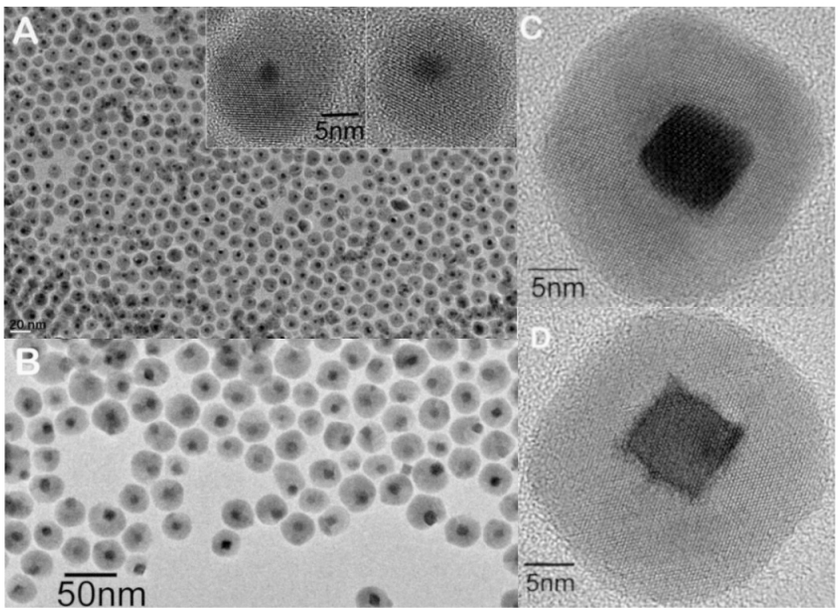

Figure 10. Core/shell metal–semiconductor NCs with thick monocrystalline CdS shell synthesized by PPh_3 initialization under large lattice mismatches: LRTEM and HRTEM images of Au–CdS NCs (A) and Pt–CdS NCs with Pt nanocube core (B-D). Adapted from Gui et al. [31] with permission; copyright Wiley-VCH Verlag GmbH & Co. KGaA)

Recently, through the strategy in Figure 5C, Zhang et al. have demonstrated evolution of relative position of Au and CdX in Au–CdX (X means S, Se, and Te) from symmetric to asymmetric configuration (Figures 12 and 13) [32].

http://dx.doi.org/10.5772/61888

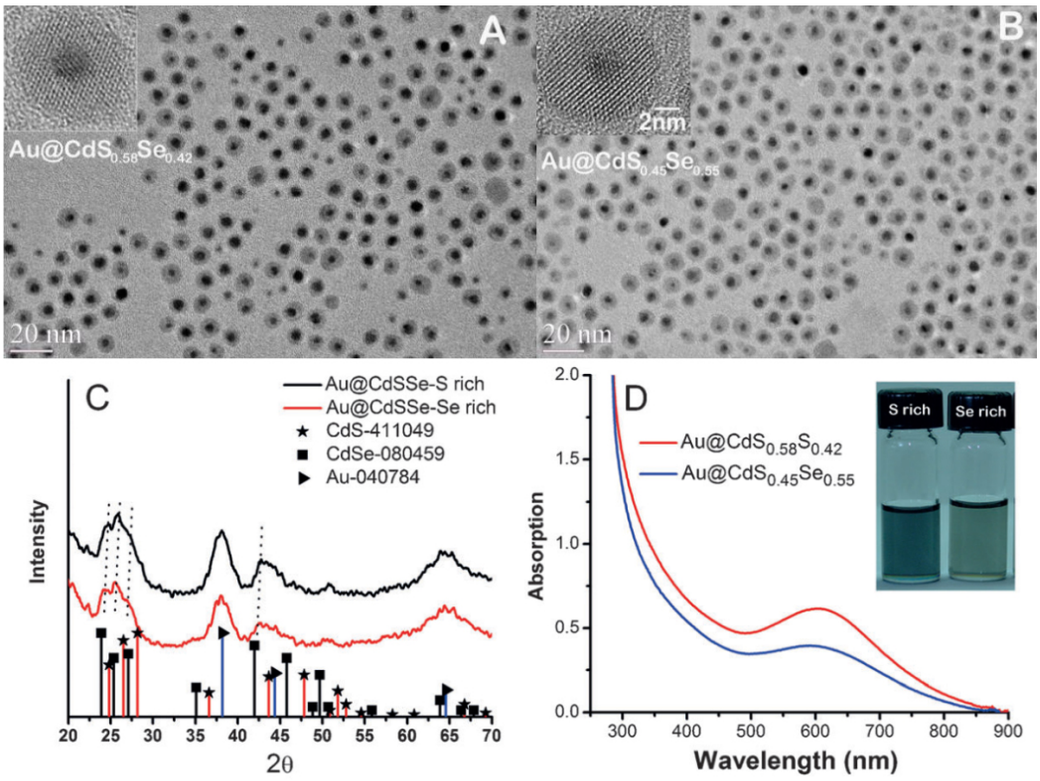

Figure 11. Au–$CdS_{1-x}Se_x$ NCs synthesized by PPh_3 initialization. (A, B) LRTEM and HRTEM images of prepared Au–$CdS_{0.58}Se_{0.42}$ NCs and Au–$CdS_{0.45}Se_{0.55}$ NCs. (C) XRD patterns comparison of them. (D) UV-Vis extinction spectra comparison of them. Inserted pictures showed their colloid color. Adapted from Gui et al. [31] with permission; copyright Wiley-VCH Verlag GmbH & Co. KGaA)

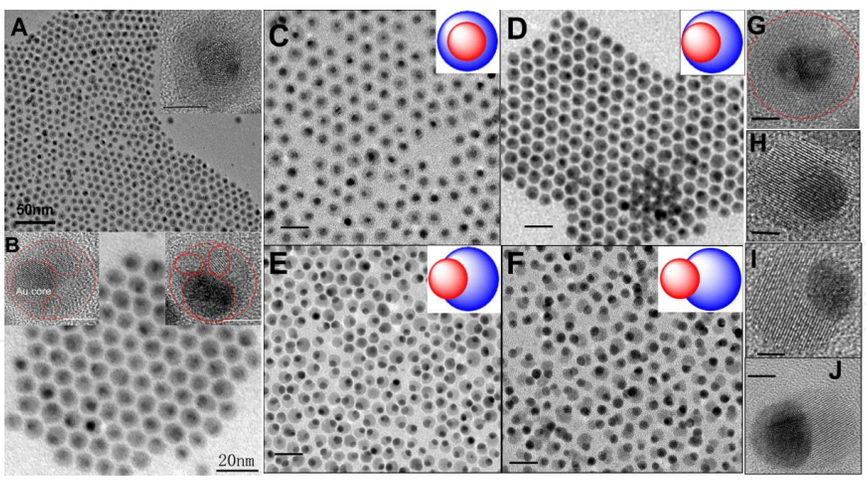

Figure 12. TEM characterizations on controllable structural symmetry from core/shell to heterodimers. (A, B) Au–Ag_2S with amorphous (A) and crystalline Ag_2S (B) shells. The inserts are HRTEM images of a-Ag_2S (A) and c-Ag_2S shell (B); scale bar, 5 nm. Red solid lines are guides for the eye, distinguishing the Au core and c-Ag_2S shell boundaries, respectively. (C–F) Au/CdS hybrid nanostructure with controllable structural symmetry. (C) Concentric core/shell. (D) Non-concentric core/shell. (E, F) Heterodimers. The inset diagrams highlight the phase separation-induced Au/CdS morphologies. Scale bar: 20 nm. (G–J) HRTEM images highlight the shape separations of panels C–F, respectively. Scale bar: 2.5 nm. Adapted from Zhao et al. [32] with permission; copyright Wiley-VCH Verlag GmbH & Co. KGaA.

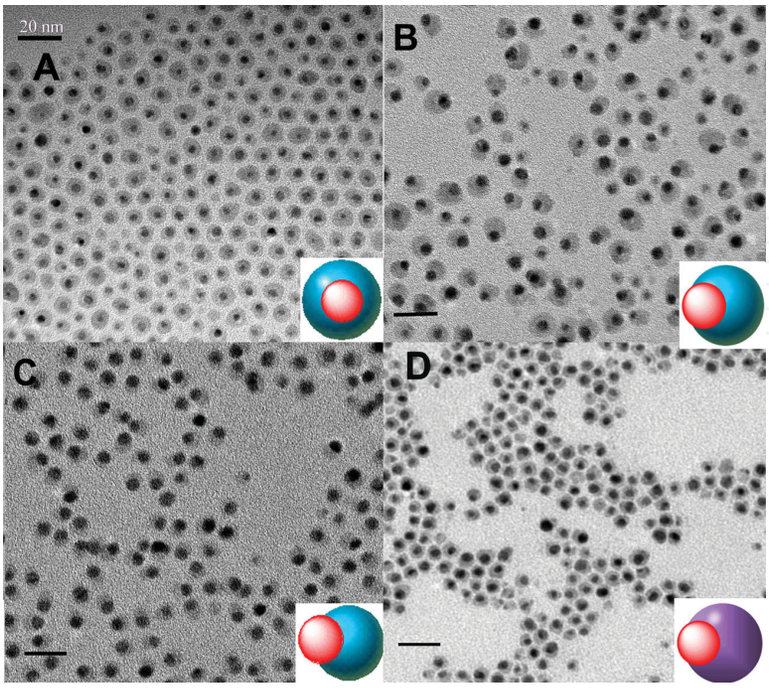

Figure 13. Large-scale TEM images of shape evolutions in Au/CdSe and Au/CdTe hybrid nanostructures with ~5 nm sized Au. (A) Concentric core/shell of Au/CdSe; (B, C) heterodimer of Au/ CdSe; (D) heterodimer of Au/CdTe. The inset diagrams highlight the phase separation-induced Au/CdSe and Au/CdTe morphologies. Scale bar: 20 nm. Adapted from Zhao et al. [32] with permission; copyright Wiley-VCH Verlag GmbH & Co. KGaA.

Based on Figure 5, the metal/semiconductor core/shell NCs can further lead to fine tuning of plasmon–exciton coupling, different hydrogen photocatalytic performance, and enhanced photovoltaic, electrical properties.

2.4. Metal/semiconductor yolk/shell nanocrystals

With a unique structure, metal-semiconductor yolk/shell nanocrystals play an important role in photocatalysis and other fields [56–63]. As photocatalysts, metal-semiconductor yolk/shell nanocrystals process some advantages, such as stronger absorption, higher catalysts selectivity, and higher quantum yield. Nowadays, different kinds of metal-semiconductor yolk/shell nanoarchitecture have been designed to enhance their photocatalysis properties. Following it are several methods for preparing metal-semiconductor yolk/shell nanocrystal.

2.4.1. Template Free for formation of metal/semiconductor yolk–shell nanocrystals

Following this method, metal/semiconductor yolk–shell nanocrystals are synthesized directly. During the process, no any nanostructure is used as template or core–shell nanocrystals forming during the process are taken as self-template [56, 64, 65]. For example, Pt–CeO_2 yolk–shell nanoparticles can be synthesized by hydrothermal method, although the mechanism may involve several factors [64]. Pt nanoparticles and CeO_2 precursors are put into the autoclave and heated at 90ºC in a period. The authors illustrate that the ratio of $CeCl_3$ concentration and

http://dx.doi.org/10.5772/61888

Pt colloid solution is the main factor to formation of yolk–shell nanoparticles. Only can Pt–CeO_2 core–shell nanoparticles be obtained when a larger $CeCl_3$/Pt ratio is employed. With a smaller ratio, the looser shell of Pt–CeO_2 yolk–shell nanoparticles can be obtained. The yolk–shell nanoparticles enhance the properties of photocatalysis of hydride of Pt and CeO_2.

Au–Cu_2O yolk–shell nanocrystals are synthesized by prolonging the reaction time after formation of Au–Cu_2O core–shell nanocrystals [65]. Cu_2O shell grows on the surface of Au nanoparticles to form Au–Cu_2O core–shell nanoparticles. As the reaction time increasing, Au core and Cu_2O shell spare forming yolk–shell nanostructure. The longer the reaction time, the more obvious the yolk–shell nanostructure. Furthermore, the thickness of Cu_2O shell can be tuned with Au colloid/Cu^{2+} ratio. As the authors showed in the articles, the distance between Au core and Cu_2O shell and the thickness of Cu_2O shell have a strong influence on the optical properties of Au–Cu_2O yolk–shell nanoparticles (Figure 14). It means that the method for preparation of Au–Cu_2O with tunable yolk–shell nanoparticle provides a route to tune the optical properties which is of importance for photocatalysis.

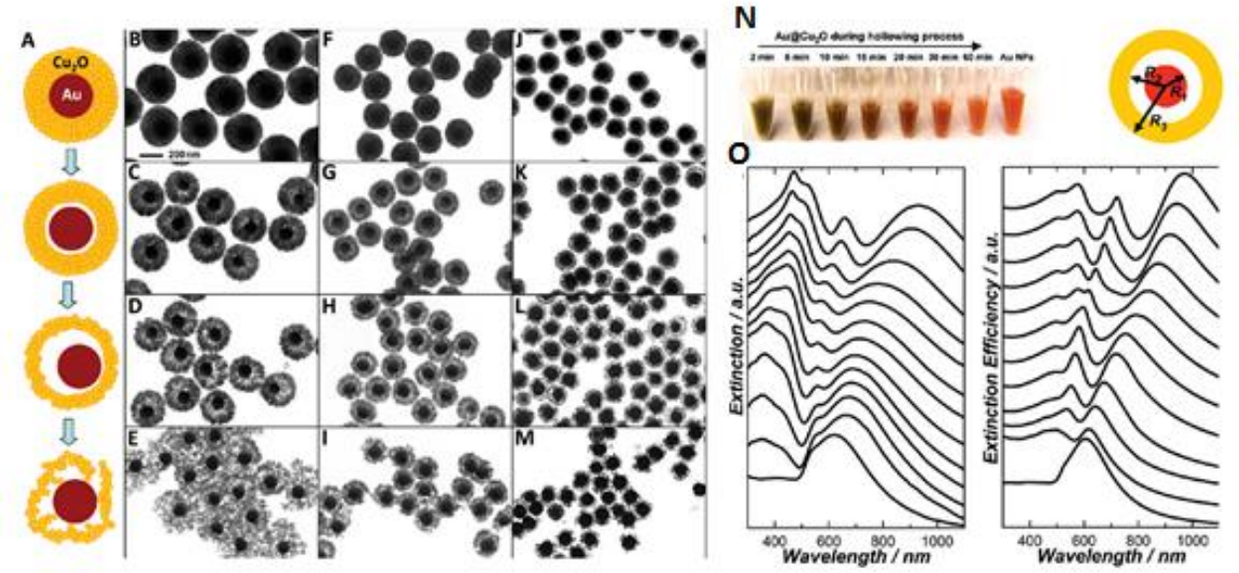

Figure 14. (A) Schematic illustration of formation of Au–Cu_2O yolk–shell nanocrystals. (B–M) TEM images of prepared Au–Cu_2O yolk–shell nanoparticles. (N) Photograph of Au–Cu_2O during hollow process. (O) Their optical properties collected by experiment and simulation. Copyright: American Chemistry Society, 2011.

Co–SiO_2 yolk–shell nanoparticles are obtained by reduction of CoO–SiO_2 core–shell nanoparticles. Park et al. coat silica on CoO nanoparticles to form CoO–SiO_2 nanoparticles then reduce CoO–SiO_2 nanoparticles with hydrogen to form Co–SiO_2 yolk–shell nanoparticles [66].

With template free method, some metal cation is introduced into hollow nanocrystals then reduced forming metal nanoparticles in the cavities of hollow structure [67, 68]. Cu–SiO_2 yolk–shell nanocrystal is synthesized by reducing Cu^{2+} cation in cavity of SiO_2 hollow particle and the size of Cu core can be tuned by multiple reduction cycles (Figure 15A–D) [67]. Besides that,

yolk–shell nanocrystals can be employed because they also have cavities for reduction of metal cation. By this method, multiplied cores or cores with different materials can be synthesized. Au–SiO_2 yolk–shell with tunable core is prepared by reducing HAuCl4 in the cavity of SiO_2–SiO_2 yolk–shell nanostructure (Figure 15F–I) [68]. On account of that, metal cation can be introduced into the cavities of hollow nanoparticles or yolk–shell nanoparticles, and other kinds of metal cation can be introduced into the cavities to react with metal core forming a new metal core or alloy core. For instance, Ag–SiO_2 yolk–shell nanoparticles can be obtained by displacing Cu with Ag^+ from Cu–SiO_2 yolk–shell nanoparticles (Figure 15E) [67]. Moreover, because the cavity of yolk–shell can be taken as reactor, the synthesis way can be applied to form other yolk–shell nanostructures.

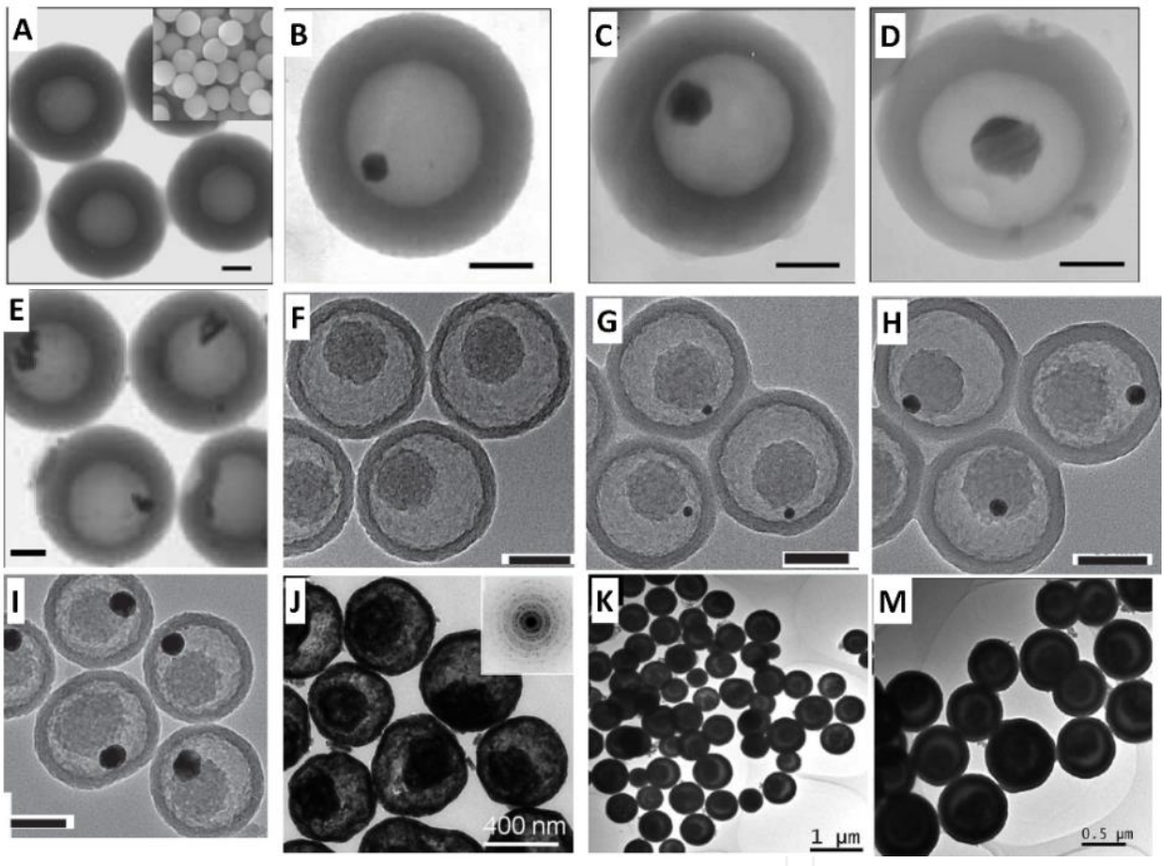

Figure 15. TEM images of various yolk–shell nanoparticles prepared with different way. (A) SiO_2 hollow nanosphere, (B–D) Cu–SiO_2 yolk–shell nanoparticles, and (E) Ag–SiO_2 yolk–shell prepared by replacing the Cu core of Cu–SiO_2 yolk–shell nanoparticles with Ag+; scale bar: 100 nm [67]. Copyright: Royal Society of Chemistry, 2004. (F) SiO_2–SiO_2 yolk–shell nanoparticles, (G-I) Au–SiO_2 yolk–shell nanoparticles with different sizes Au core; scale bar: 50 nm [68]. Copyright: Wiley-VCH, 2010. (J) Au–CeO_2 yolk–shell nanoparticles [69]. Copyright: RSC, 2012. (K-M) Pt–CeO_2 yolk–shell nanoparticles [64]. Copyright: RSC, 2011.

Although some of mechanism of template free of yolk–shell nanostructure formation is unclear, it provides the method to design and prepare metal/semiconductor yolk–shell nanocrystals.

http://dx.doi.org/10.5772/61888

2.4.2. Using template for metal-semiconductor yolk–shell nanocrystals

Template employed for synthesizing metal-semiconductor yolk–shell nanocrystals can be conclude into two kinds of templates: soft template and hard template.

Using soft template for metal-semiconductor yolk–shell nanocrystals: By soft template protocol, several kinds of chemical are usually employed as soft template, such as biomolecular, polymers, surfactants, or microemulsions [56, 70]. In most of case, the large molecular would form microemulsions in solution and precursors react on the boundary of microemulsions. Therefore, sizes or morphologies of yolk–shell nanoparticles could be tuned by tuning cell of microemulsions [71–73]. For metal semiconductor yolk–shell nanoparticles, metal core is reduced in the cavities of microemulsions then semiconductor shell grows on the boundary of microemulsions. For instance, Priebe and Fromm synthesize the Ag–SiO_2 yolk–shell nanoparticles in cyclohexane and Igepal CO-520 system [72]. Ag^+ is introduced into cavity of microemulsions and reduced to nanoparticles. Subsequently, silica precursor is introduced into the system and form the shell on the boundary of microemulsions (Figure 16). Besides, because Ag^+ is reduced in the cavities, the size of Ag core can be tuned by using the series of concentration of $AgNO_4$ solution.

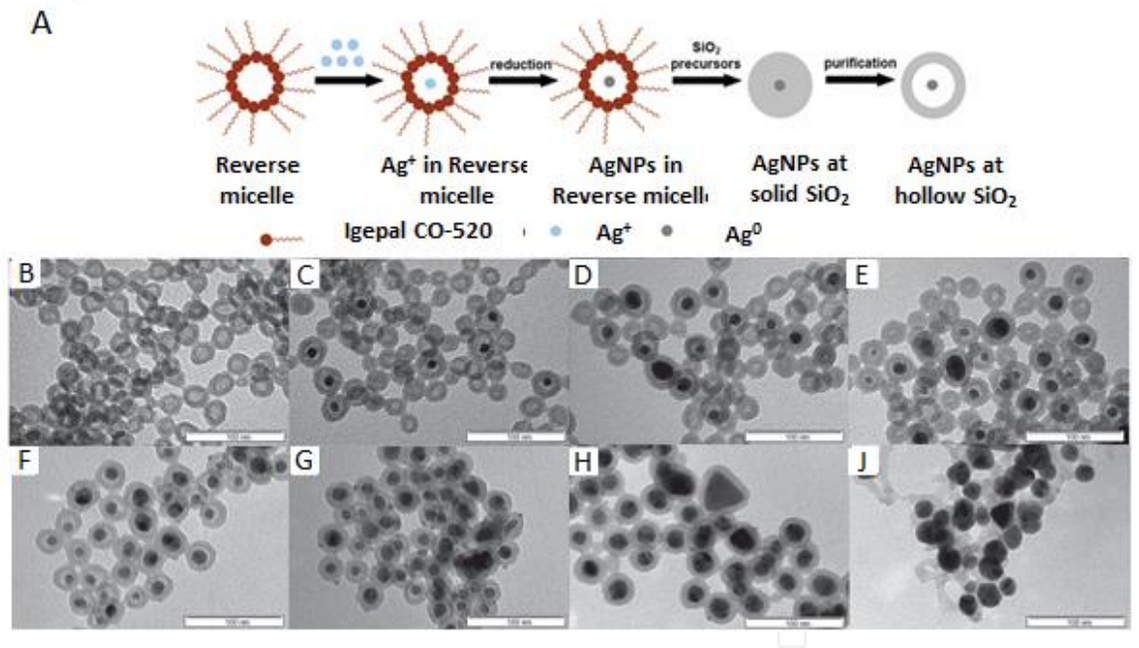

Figure 16. (A) Schematic for formation of Ag–SiO_2 yolk–shell nanoparticles and (B–I) TEM images of Ag–SiO_2 yolk–shell nanoparticles with various Ag core size; scale bar: 500 nm, Copyright: Wiley-VCH, 2014.

Metal cores can also be introduced the cavities of microemulsions and then the shell grows to form metal/semiconductor yolk–shell nanoparticles directly [73]. Hyunjoon Song and his coworkers introduce Pd nanoparticles into the system of hexanol and igepal CO-630, followed by adding tetraethyl orthosilicate (TMOS) and octadecyltrimethoxysilane (C18TMS) for shell growth (Figure 17). Their protocol provides a possible method for preparing metal/semiconductor yolk–shell nanoparticles with other metal core and semiconductor shell.

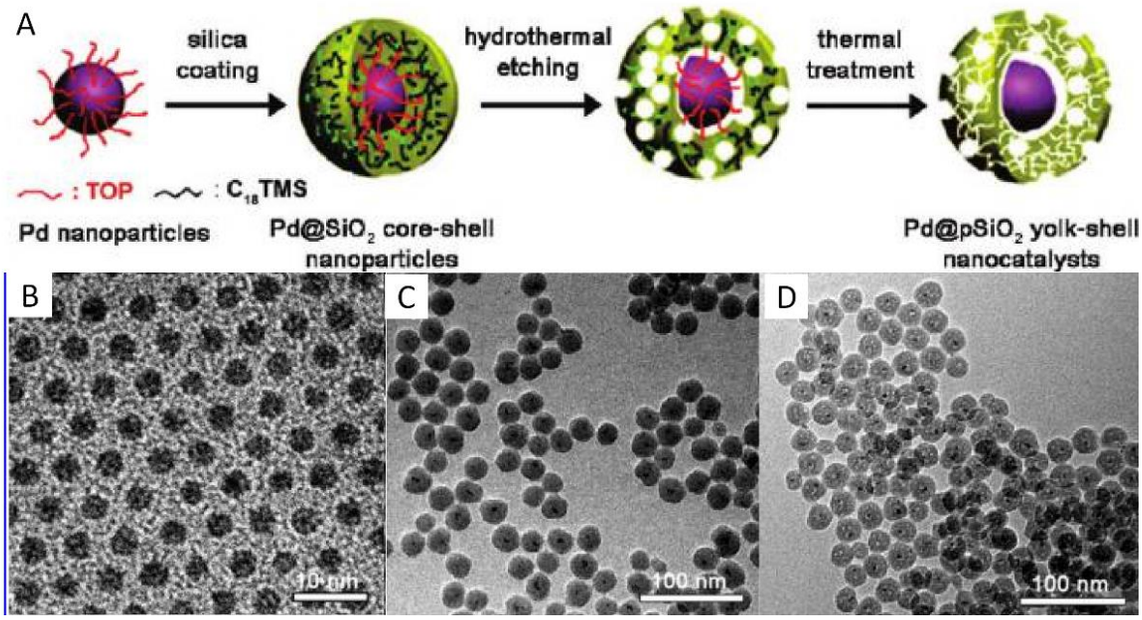

Figure 17. (A)Schematic for preparing Pb–SiO_2 yolk–shell nanoparticles and TEM images of Pb cores (B), Pb–SiO_2 core–shell nanoparticles (C), and Pb–SiO_2 yolk–shell nanoparticles(D). Copyright: ACS, 2011.

Using hard template for metal/semiconductor yolk–shell nanostructure: By hard template method, shell coating on core is synthesized as middle layer and subsequently removed or etched. The material of middle shell includes SiO_2, carbon, polymer, and so on. For example, Au–TiO_2, Au–ZrO_2, Au–SnO_2, and Au–SiO_2 yolk–shell nanoparticles are synthesized by coating semiconductor shell on Au–oxides and subsequently etching oxides layer (Figure 18) [74–77]. In most of case, SiO_2 is employed as hard template to form the middle layer and etched by NaOH, HF, or other reagents.

For example, Au–ZrO_2 yolk–shell nanoparticles can also be synthesized by etching SiO_2 layer of Au–SiO_2–ZrO_2 core–shell nanoparticles (Figure 18A) [74]. It is reported that such Au–ZrO_2 yolk–shell nanostructure is stable at high temperature and can be used as catalyst for the oxidation of CO. Taking SiO_2 as template, SnO_2 hollow nanosphere, and Au–SnO_2 yolk–shell nanoparticles can be obtained (Figure 18B). Lou et al. show their work on preparation of Au–SnO_2 yolk–shell nanoparticles, etching the SiO_2 layer with HF and they found that controlling the size of SiO_2 template cage-like and double layer shell of Au–SnO_2 can be obtained [75]. The method can also be used for synthesis of yolk–shell with other hybrid material shell [78].

3. The photocatalytic hydrogen evolution applications of metal/semiconductor hybrid nanocrystals

3.1. Mechanism of photocatalysis on semiconductors and key problems

Since Fujishima and Honda [79] discovered photoelectrochemical formation of H_2 over TiO_2 electrode, photocatalytic water splitting and H_2 evolution are an attractive solution of global

http://dx.doi.org/10.5772/61888

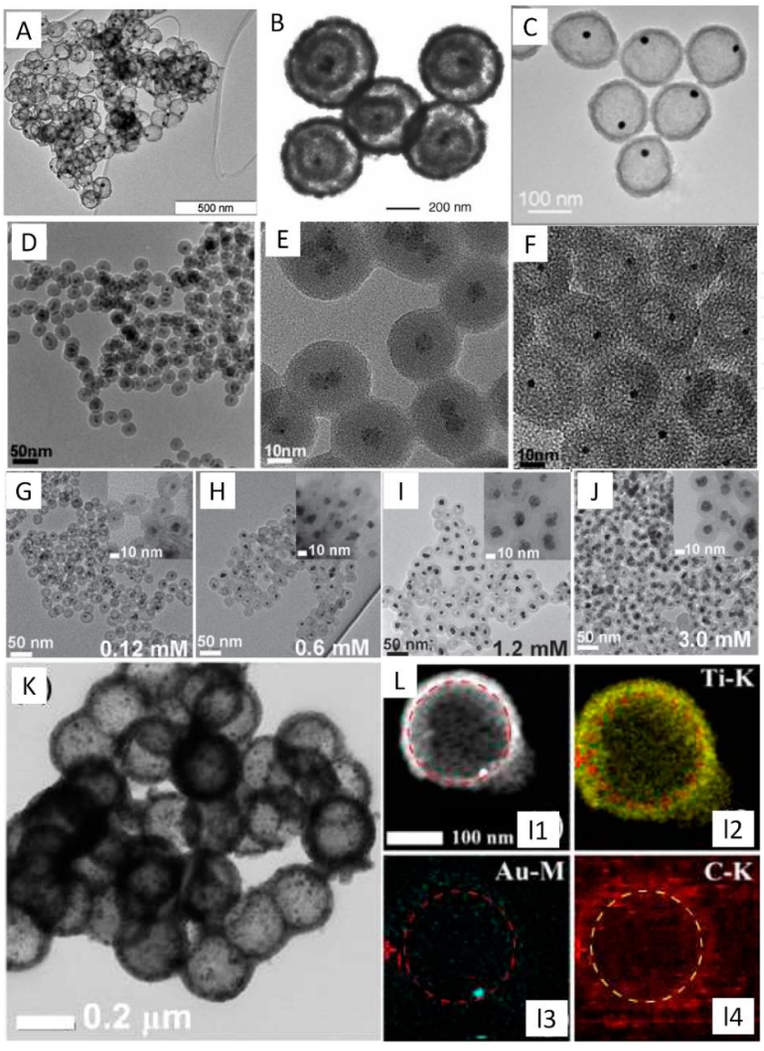

Figure 18. TEM images of (A) Au–ZrO_2 yolk–shell nanoparticles [74]. Copyright: Wiley-VCH, 2006. (B) Au–SnO_2, yolk–shell nanoparticles [75]. Copyright: Wiley-VCH, 2007. (C) Au–Zr0.5Si0.5O_2 yolk–shell nanoparticles [76]. Copyright: Springer, 2014. (D, E) $Fe3O_4$/Au–SiO_2 yolk–shell nanoparticles. (F) Au–SiO_2 yolk–shell nanoparticles. (G–J) Ag–SiO_2 yolk–shell nanoparticles [77]. Copyright: Royal Society of Chemistry, 2010. (K, L) TEM and HAADF-STEM images and EDS maps of Au–GO/TiO_2 yolk–shell nanoparticles [78]. Copyright: America Chemistry Society.

energy supply and related environmental issues. Numerous researchers had extensively studied water splitting using semiconductor photocatalysts since the finding [80–87]. The fundamental principle of solar water splitting for semiconductor photocatalysts is shown in Figure 19. Semiconductor materials have a band structure in which the conduction band (CB) is separated from the valence band (VB) by a band gap with a suitable width. When the energy of incident light is larger than that of a band gap, the electrons in the VB of the semiconductor photocatalyst are excited to the CB, while the holes are left in the VB. Therefore, it creates the negative-electron (e-) and the positive-hole (h+) pairs. These photogenerated electron–hole pairs may further be involved in the following possible processes: (1) successfully migrate to the surface of semiconductor, (2) be captured by the defect sites in bulk and/or on the surface region of semiconductor, and (3) recombine to release the energy in the form of heat or photon.

If the photoexcited carriers separate and migrate to the surface without recombination, adsorbed species are reduced and oxidized by the photogenerated electrons and holes to produce H_2 and O_2, respectively (Figure 19).

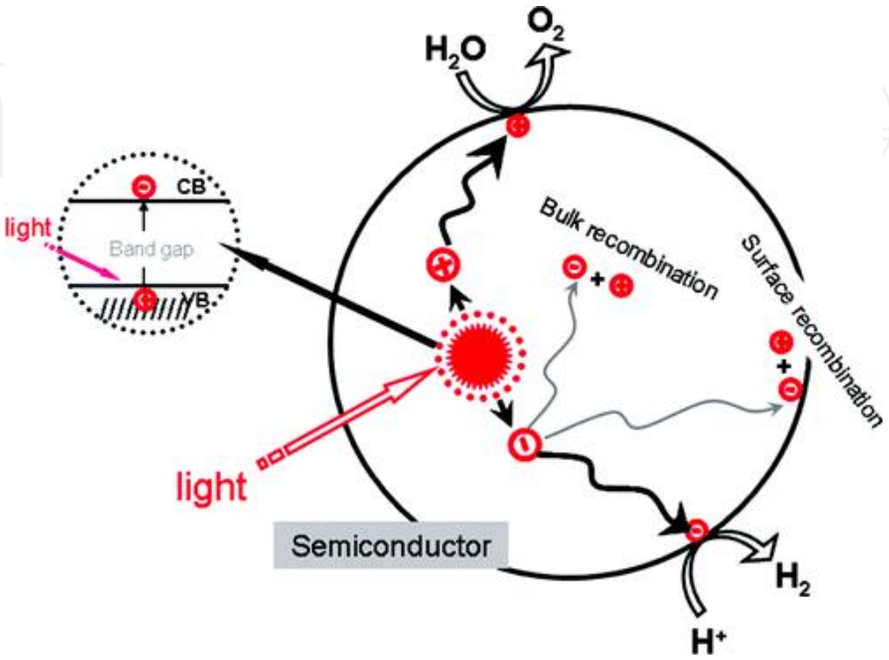

Figure 19. Process in photocatalytic water splitting [80]. Copyright: Royal Society of Chemistry, 2009.

For effective water splitting, important points in the semiconductor photocatalyst materials are their band structure, including the band gap and positions of VB and CB. The bottom level of the CB has to be more negative than the redox potential of H^+/H_2 (0 V vs. NHE), while the top level of the VB be more positive than the redox potential of O_2/H_2O (1.23 V) [80]. Therefore, a minimum band gap of 1.23 eV is required, while a much larger band gap (usually >2.0 eV) is often needed for appreciable water splitting reaction due to additional overpotential associated with each electron transfer and gas evolution step [84]. The band edge positions of some semiconductor photocatalysts are shown in Figure 20. The band structure of a semiconductor is not only determined by its own crystal phase and vacancies but can also be modified by the introduction of foreign elements into the bulk or surface of the semiconductor. Take the most studied photocatalyst TiO_2 as an example, the larger band gap (~3.2 eV) of TiO_2 limits its utilization of the solar spectrum to only the ultraviolet (UV) region (wavelength $\lambda < 400$ nm) [85]. The solar spectrum has a very small fraction of UV light (ca. 5%) in comparison with those of visible light ($400 < \lambda < 800$ nm, ca. 43%) and near-infrared (NIR) light ($800 < \lambda < 2500$ nm, ca. 52%) [83]; therefore, studies on visible-light-driven photocatalysts are more important for practical applications. There are two efficient strategies to make TiO_2 as visible-light-driven photocatalysts as shown in Figure 2B [84]: (1) narrow the band gap of TiO_2 to make it absorb visible light by introducing other elements into TiO_2 and (2) modify the TiO_2 surface with other visible light active materials (dye or quantum dot) as a light harvester to sensitize TiO_2.

http://dx.doi.org/10.5772/61888

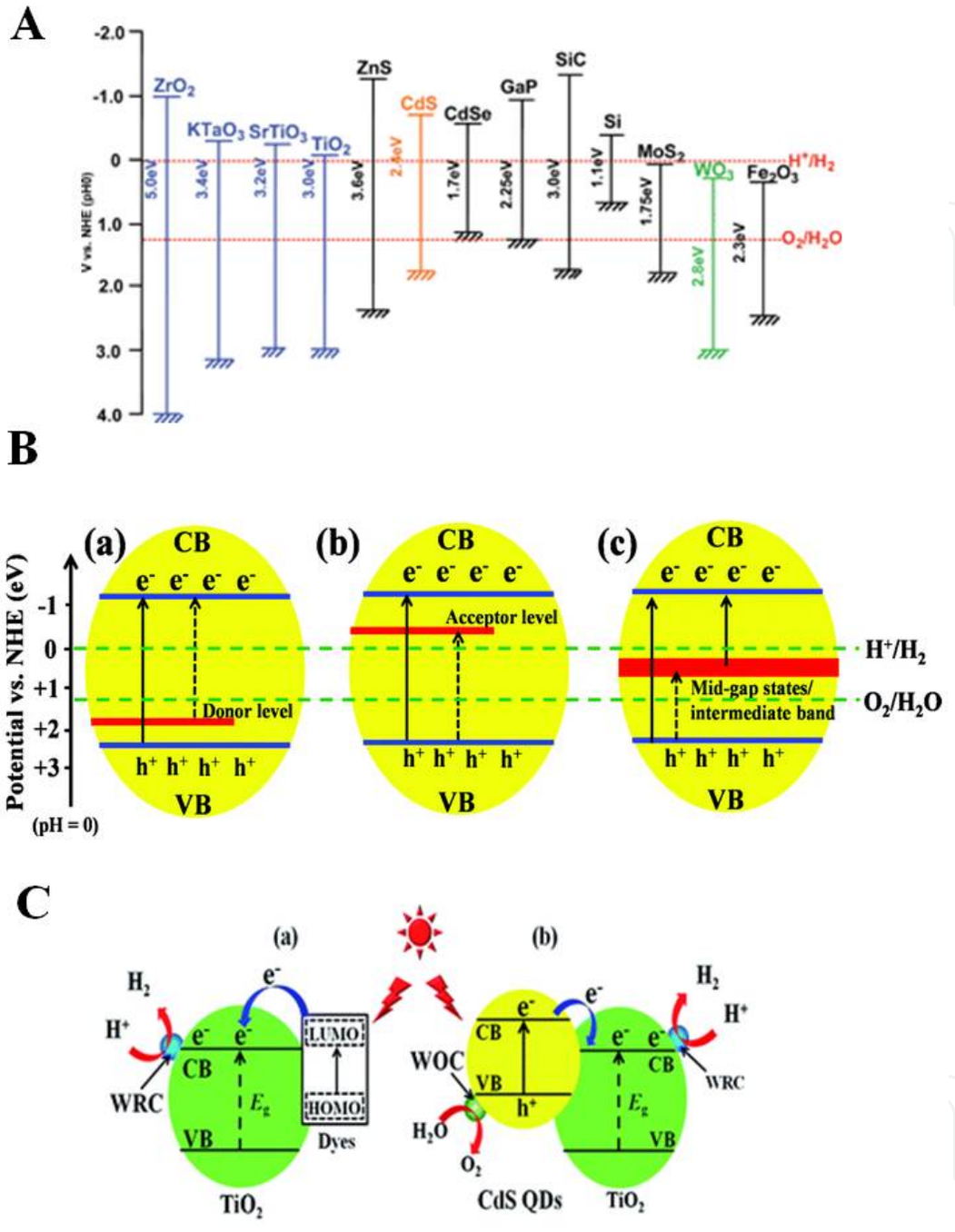

Figure 20. (A) Relationship between band structure of semiconductor and redox potential of water splitting [80]. Copyright: Royal Society of Chemistry, 2009. (B) Donor level (a), acceptor level (b), and mid-gap states (c) formed by metal ion doping. (C) The mechanism of H2 production for (a) dye-sensitized and (b) QDs-sensitized semiconductor [82]. Copyright: Royal Society of Chemistry, 2015.

After excited charges are created, efficient charge separation is next crucial factor determining the light to fuels conversion efficiency. Crystal structure, crystallinity, and particle size strongly affect the step [86]. The defects operate as trapping and recombination centers between

photogenerated electrons and holes, resulting poor photocatalytic activity. Therefore, improving the crystalline quality will decrease the amount of defects and improve photocatalytic activity. If the particle size becomes small, the distance that photogenerated electrons and holes have to migrate to reaction sites on the surface becomes short, and this results in a decrease in the recombination probability. Also, the fabrication of junction structure has been recognized as an effective strategy to avoid charge recombination in semiconductors.

The surface catalytic reaction is a successive step of charge separation. The important points for this step are surface character (active sites) and quantity (surface area). Even if the photogenerated electrons and holes possess thermodynamically sufficient potentials for water splitting, they will have to recombine with each other if the active sites for redox reactions do not exist on the surface. Cocatalysts such as Pt, NiO, and RuO_2 are usually loaded to introduce active sites for H2 evolution [87], which will be discussed later.

The processes of the photocatalytic reaction on a semiconductor photocatalyst involve light absorption, charge separation, carrier migration, and surface catalytic reactions. Therefore, developing band gap engineering to narrow down the band gap of semiconductor materials for absorbing broader spectrum of solar energy and materials engineering to tune the physical properties (crystal structure, crystallinity, and particle size) for gaining efficient charge separation and migration and creating enough active sites are the key problems of improving photocatalytic hydrogen evolution efficiencies.

3.2. Metal/semiconductor heterodimer nanocrystals: the role of metal

Integration with metal is a commonly used configuration to improve the photocatalytic hydrogen evolution performance of a semiconductor. The metal may play a variety of roles in the enhancement of photocatalytic performance. In the following sections, we will focus on the role of metal as cocatalyst and the plasmonic effect of noble metals.

3.2.1. The cocatalyst role

Since the work by Kraeutler and Bard in 1978 loading Pt on the surface of TiO_2 [88], the loading of metal nanoparticles onto different semiconductor photocatalysts has been regarded as a popular strategy to improve the photocatalytic performance in photocatalytic water splitting. Besides Pt, other metal cocatalysts, including Pd, Rh, Ru, Ir, Ag, Ni, Co, etc., have been recognized as efficient cocatalysts for photocatalytic hydrogen evolution [89–96]. The processes of charge transfer between metal cocatalyst and host semiconductor photocatalyst are described in Figure 21A.

The metal cocatalysts mainly play two roles in the improvement of photocatalytic performance. One is to assist in electron–hole separation through the formation of Schottky barrier between the metal cocatalyst and the light-harvesting semiconductor. A Schottky barrier is a type of junction resulting from the intimate contact of a metal with a semiconductor (Figure 21B). The metal cocatalyst with larger work function, that is, lower Fermi energy level, should more readily trap the photogenerated electrons migrated to the surface of the host semiconductor photocatalyst. Meanwhile, the photogenerated holes stay at the host photocatalyst and

http://dx.doi.org/10.5772/61888

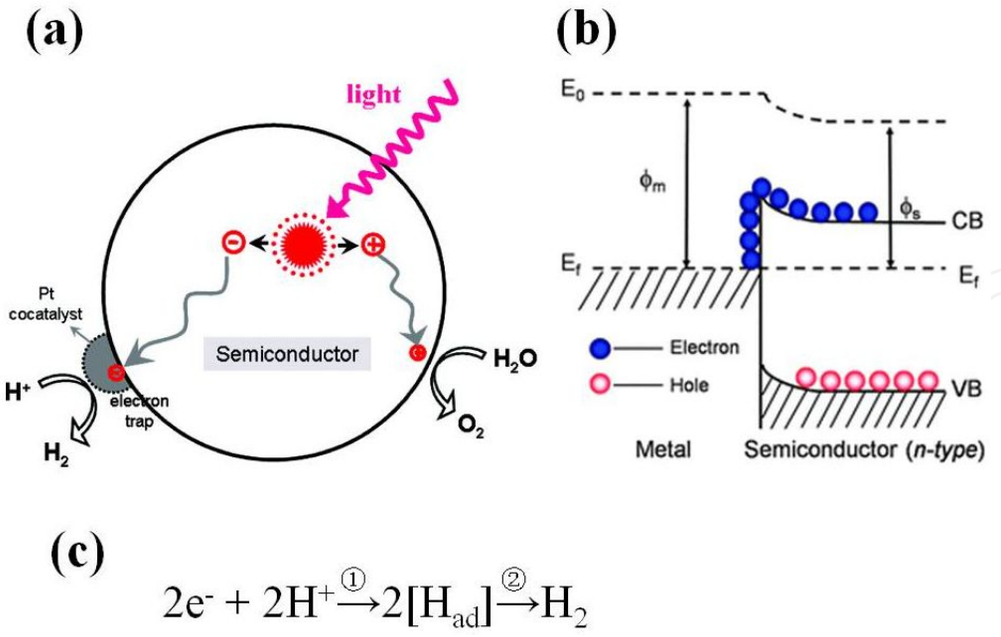

Figure 21. (A) Processes of charge transfer between host photocatalyst and cocatalyst, taking Pt as the example of cocatalyst [86]. Copyright: America Chemistry Society, 2010. (B) Schematic of Schottky barrier [90]. Copyright: Royal Society of Chemistry, 2010. (C) Two general steps for proton reduction reaction [89]. Copyright: America Chemistry Society, 2013.

migrate to its surface. This retards the possibility of electron–hole recombination and enhances efficient separation of the photogenerated electrons and holes. It improved the overall photocatalytic activity of the water splitting because it helps to promote charge separation, which in return reduces both bulk and surface electron/hole recombination.

The other role of metal cocatalysts is to serve as the reaction sites to catalyze the proton reduction to H_2. Proton reduction course on cocatalysts goes through at least two steps: a discharge step and catalytic step (Figure 21C) [89]. Most semiconductor photocatalyst, particularly oxides, lack surface H_2 evolution sites rather than O_2 evolution sites since their CB levels are not sufficiently negative for electrons to reduce water to produce H_2 without catalytic assistance whereas their VB levels are usually positive enough for holes to oxidize water and form O_2 even in the absence of cocatalyst [92]. Metal cocatalysts could lower the activation energy or overpotential for H_2 evolution reaction on the surface of semiconductors. It also accelerates the surface chemical reaction by inhibiting the backward reaction.

Overall, the role played by the metal cocatalysts dispersed on the surface of the semiconductor photocatalysts is extremely important. Many factors can affect the capability of H_2 evolution cocatalysts in the semiconductor-based photocatalytic water splitting, such as cocatalyst loading amount and its particle size and structure [89, 94]. For example, there is a volcano-type trend between the loading amount of a given cocatalyst and the photocatalytic activity (regardless of the synthesis method, photocatalyst type, and loaded cocatalyst) [94, 95]. At the same loading amount, metal cocatalysts with smaller size and high dispersion display higher catalytic activity due to their larger specific surface area and more active sites [96].

3.2.2. The plasmonic metal case: plasmonic-metal/semiconductor heterodimer nanocrystals

The harvesting and conversion of solar energy become a renewed in recent years. Among various technologies, the direct conversion of solar to chemical energy using photocatalysts has received significant attention. Although heterogeneous photocatalysts are almost exclusively semiconductors, it has been demonstrated recently that plasmonic nanostructures of noble metals (mainly silver and gold) also show significant promise [1]. Herein, the recent progress in using plasmonic metallic nanostructures in the field of photocatalysis is reviewed. We focus on plasmon-enhanced water splitting on composite photocatalysts containing semiconductor and plasmonic-metal building blocks and recently reported plasmon-mediated photocatalytic reactions on plasmonic nanostructures of noble metals.

Plasmonic metallic nanostructures are characterized by their strong interaction with resonant photons through an excitation of surface plasmon resonance (SPR). SPR can be described as the resonant photon-induced collective oscillation of valence electrons, established when the frequency of photons matches the natural frequency of surface electrons oscillating against the restoring force of positive nuclei (Figure 22A). The resonant photon wavelength is different for different metals. For example, gold, silver, and copper nanostructures exhibit resonant behavior when interacting with ultraviolet (UV) and visible (Vis) photons. The utilization of the localized SPR (LSPR) effect of nanostructured Au, Ag, and Cu was examined for the potential photocatalysis [97–99], using Au or Ag nanoparticles (NPs) supported on ZrO_2, AgCl, or TiO_2 for the unselective degradation of organic species under visible light irradiation. As shown in Figure 22 A, LSPR is the resonant photon-induced coherent oscillation of charge at the metal-dielectric interface, established when the photon frequency matches the natural frequency of metal surface electrons oscillating against the restoring force of their positive nuclei [100]. The frequency of the surface plasmon absorption is highly dependent on the type of metal, size, shape, surrounding dielectric medium, distance between neighboring objects, and configuration their ensemble [101]. A wide range of metal/semiconductor heterostructures, including Au/TiO_2, Ag/TiO_2, Au/CdS, and Au/Fe_2O_3, have been explored to achieve enhanced photocatalytic activity [102–110].

Although the exact nature of LSPR effect on enhanced photocatalytic activity is not entirely understood, three possible enhancement mechanisms have been proposed: (1) near-field enhancement, (2) SPR-induced electron transfer from metal to semiconductor, and (3) scattering [103, 104] (Figure 22A–C). The strong SPR-induced electric field of plasmonic metal NPs can interact with the adjacent semiconductor (Figure 22B-a), this interaction may increase the rate of exciton formation and the concentration of the charge carriers generated in this part of the semiconductor [104]. If only the metal excited, the metallic plasmonic NPs can absorb resonant photons and transfer energetic photogenerated charge carrier to the semiconductor during the decay of the LSPR (Figure 22B-b). As a result of the plasmonic sensitization process, a wide band gap semiconductor could perform catalytic reduction reactions under visible light. Plasmonic structures of size larger than 50 nm are efficient in scattering the resonant photons, which increases the path length of photons in semiconductor/plasmonic metal nanostructures. Therefore, the resonant photons that are not absorbed by semiconductor photocatalysts could be scattered by the bigger plasmonic metal particles, ultimately increasing the number of

http://dx.doi.org/10.5772/61888

electron/hole pairs. The above-mentioned three mechanisms are governed by the metal/semiconductor configurations and their arrangements in the hybrid system.

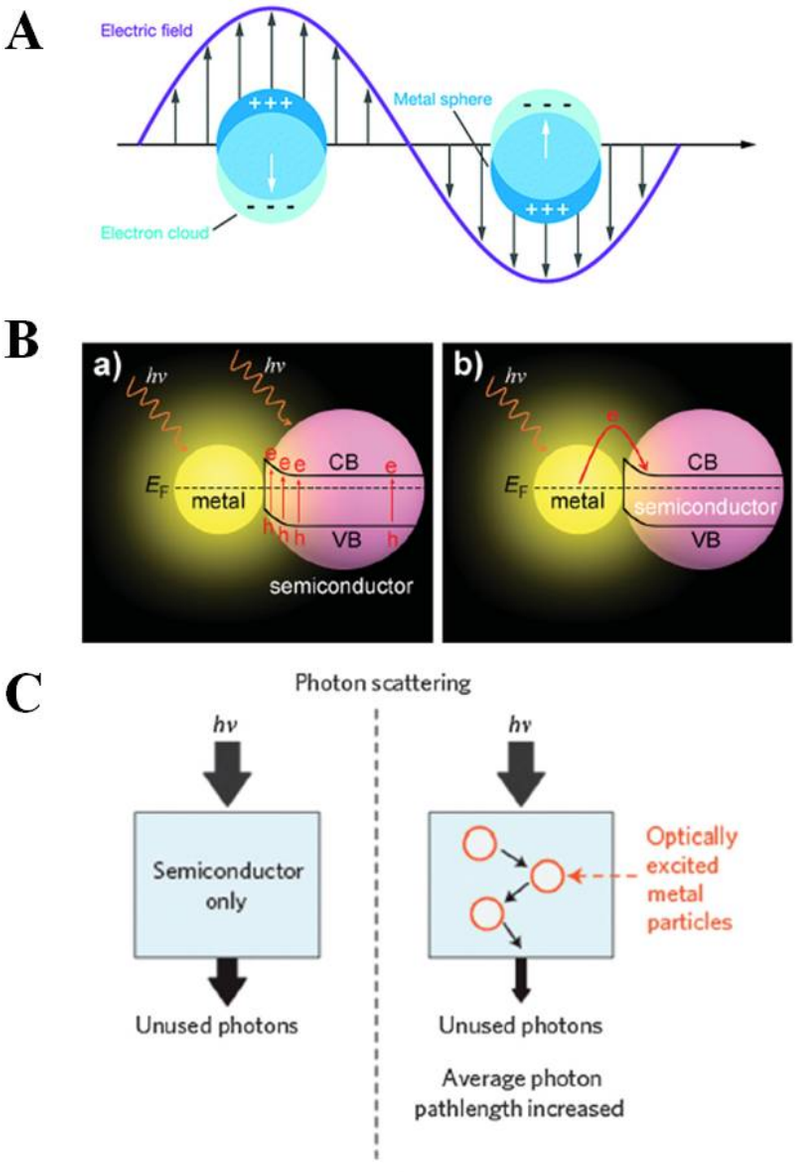

Figure 22. Schematic illustrating (A) localized surface plasmon resonance [102]. Copyright: America Chemistry Society, 2011. (B) The mechanisms for plasmon-enhanced chemical reactions with metal/semiconductor hybrid nanostructures: (a) plasmonic enhancement of light absorption; (b) hot-electron effect [103], with permission. Copyright Wiley-VCH Verlag GmbH & Co. KGaA. (C) The scattering mechanism [104]. Copyright: Royal Society of Chemistry, 2013.

In the case of SPR-mediated charge injection from metal to semiconductor, charge carriers are directly injected from excited plasmonic-metal nanostructures into the semiconductor surface. The metallic plasmonic nanoparticles essentially act as a sensitizer, absorbing resonant photons and transferring the energetic electron, formed in the process of the SPR excitation, to the nearby semiconductor (Figure 23) [1, 111]. Furthermore, the ability to tune the SPR

resonance wavelength and intensity by changing the size or shape of Au or Ag nanostructures suggests that plasmon enhancement could be more dramatic when the interface between Au (Ag) and semiconductor, such as TiO_2, CdS, etc. The charge injection mechanism was functional in composite photocatalysts where the plasmonic nanoparticles and semiconductor are in direct contact with each other, allowing a rapid transfer of charge carriers. These composite systems are geometrically similar to the conventional cocatalyst/semiconductor photocatalysts that are often synthesized by an incipient wetness deposition of metal precursors and their subsequent thermal treatment on a semiconductor surface. Therefore, the defect in the heterointerface should be decreased to get more efficient charge separation and injection to be "chemically useful" energetic charge carriers for photoreduction. Otherwise, too many defects on the interface will trap the photoinduced charge.

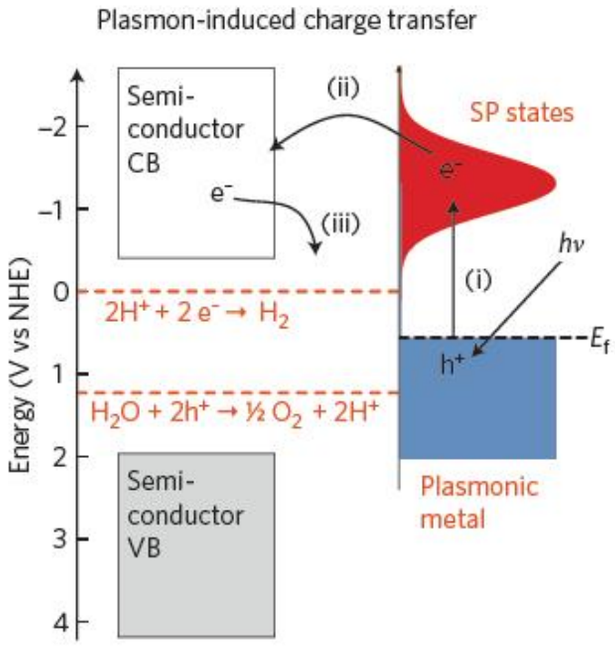

Figure 23. Mechanism of SPR-induced charge transfer with approximate energy levels on the NHE scale. Dashed red lines refer to the water-splitting redox potentials. (i) Electrons near the metal Fermi level, E_f, are excited to surface plasmon (SP) states; (ii) the electrons transfer to a nearby semiconductor particle; (iii) this activates electron-driven processes such as the hydrogen evolution half-reaction [1]. Copyright of Nature group 2011, Macmillan Publishers Limited.

3.2.3. The cocatalystic metal on semiconductor nanocrystals with well-defined crystal face exposure

Based on the photoreduction reaction of Pt^{4+} ($Pt^{4+} + e- \rightarrow Pt$) and photooxidation reaction of Pb^{2+} ($Pb^{2+} + H_2O + h^+ \rightarrow PbO_2$), it is clearly indicated that rutile {110} and {011} facets provide reduction and oxidation sites, respectively (Figure 24Aa, c) [112–113]. The obvious separation of reduction and oxidation sites on faceted rutile crystals is attributed to photoexcited electron and hole transfer between {011} and {110} facets, which is driven by the higher electronic energy levels of {011}. Although the selective distribution of photodeposited Pt and PbO_2 particles on anatase {101} and {001} facets (Figure 24 Ab, d) is not as obvious as that on different rutile

http://dx.doi.org/10.5772/61888

facets, anatase {101} and {001} facets can still be considered to be more reductive and more oxidative, respectively [113].

The spatial separation of reduction and the oxidation sites in TiO_2 crystals with appropriate different facets are well known now [114]. Consequently, the corresponding spatial separation of photoexcited charge carriers on different facets improves the photocatalytic activities of photocatalysts, as illustrated in Figure 24B and C. Liu et al. reported that anatase crystals with {101} and {001} facets, with selective deposition of Pt particles by a photoreduction process only on the reductive {101} facets show a much higher photocatalytic hydrogen evolution (reduction reaction) from a mixture of H_2O and methanol than do the same crystals with Pt particles on both {101} and {001} facets (Figure 24D). It is now clear that the difference in spatial distribution of cocatalysts on photocatalysts is an important but unfortunately neglected factor. The spatial separation of photoexcited electrons and holes on different facets was also seen in brookite nanosheets surrounded with four {210} and two {101} facts as reduction sites, and two {201} facets as oxidation sites. Consequently, such spatial separation produces an excellent photocatalytic activity of brookite, which is conventionally inactive [113–116].

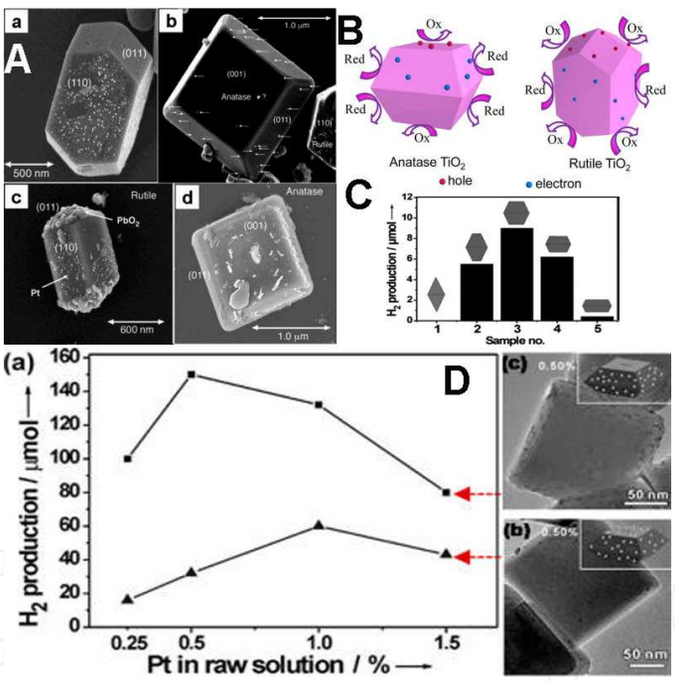

Figure 24. .(A) SEM images of (a) a rutile particle and (b) an anatase particle on which Pt fine particles were deposited by UV-irradiation in a solution of 1.0 mM H_2PtCl_6; SEM images of (c) a rutile particle and (d) an anatase particle showing PbO_2 deposits, which were loaded on the particles by UV irradiation of the Pt-deposited TiO_2 powder in a solution of 0.1 M $Pb(NO_3)_2$. Reprinted with permission from Ohno et al. [113]. Copyright 2002 Royal Society of Chemistry. (B) Schematic of the spatial separation of redox sites on anatase crystals with {101} and {001} facets and rutile TiO_2 particle with {110} and {011} facets. Reprinted with permission from Murakami et al. [115]. Copyright 2009 American Chemical Society. (C) Hydrogen production after 6 h irradiation time using TiO_2 nanocrystals (NCs) with different exposed {001} facets as photocatalysts. Reprinted with permission from Liu et al. [116]. Copyright 2013 Wiley-VCH. (D) (a) Hydrogen production amounts of Pt deposited TiO_2 NCs by means of photochemical-reduction (■) and chemical reduction routes (▲). SEM images of TiO_2 NCs with 0.5% Pt loading amount prepared by (b) chemical reduction and (c) photochemical reduction, respectively. Reprinted with permission from Liu et al. [116]. Copyright 2013 Wiley-VCH.

3.3. Metal–semiconductor core/shell nanocrystals and photocatalysis application

3.3.1. Metal core–semiconductor shell: large lattice mismatch-induced interface control and photocatalytic applications

In metal-semiconductor hetero structures, the contact interface between metal and semiconductor plays a critical role in transfer and separation of charge carriers [117–118]. Our precise symmetry control of Au–CdX can enable different contact interface between metal and semiconductor components at the nanoscale, thus offering a new dimension to control optical and electronic properties of hybrid nanostructures in a highly control manner. Figure 25A highlights evolution of plasmon–exciton coupling in Au–CdS enabled by their symmetry control. As compared with the SPR feature of a pure metal nanoparticles, optical absorption of Au–CdS is significantly broadened in the visible regime (500–700 nm), which can be attributed to the existence of plasmon–exciton coupling [119, 3]. They further performed finite-different time-domain (FDTD) simulation to evaluate optical response in Au–CdS with different structural symmetry and summarize the results in Figure 25B. The FDTD simulation reproduces symmetry dependent optical property very well. The strong SPR-induced visible light absorption of Au/CdS colloids can overlap most of the solar spectrum, and particularly important, its tunability makes it feasible to optimize photorelated processes, including solar water splitting.

It is well known that CdS or CdSe possesses conduction and valence bands at potentials appropriate for water reduction, namely, the bottoms of conduction bands locate at a more negative potential than the reduction potential of H^+ to H_2. In order to get high efficiency of H_2 evolution by sunlight irradiation, more visible light should be harvested, and then photo-excited electron/hole should be separated and migrated to the surface without recombination [120, 121]. By integrating with plasmonic Au nanoparticle in a hybrid nanostructure, its tunable optical response achieved in Figure 25A and B should make it feasible to mediate the visible light-induced electron/hole separation in CdX and electron transfer from CdX to Au surface due to the plasmon–exciton coupling [3,122]. As shown in Figure 25C and D, for comparison, photocatalysis with pure 4.5 nm CdS QDs and the CdS/Au heterodimers prepared by reported in situ deposition are also presented [123–124]. The rate of CdS QDs alone is 0.1 mmol h^{-1} g $^{-1}$.The concentric core/shell Au–CdS has the least H_2 evolution activity (0.009 mmol h^{-1} g^{-1}) and the heterodimer structured Au/CdS has better H_2 evolution activity (7.3 mmol h^{-1} g^{-1}) that manifest a dramatic photoactivity enhancement of 730 times. However, the CdS/Au heterodimers has less H_2 evolution activity (0.359 mmol h^{-1} g^{-1}). Figure 25C and D can be understood by the mechanism of SPR enhanced electron–hole separation and collection, as illustrated in the Figure 25E. For an asymmetric Au–CdS heterodimer, under visible light illumination, the energy band alignment between CdS and Au suggests a rapid electron transfer from conduction band of CdS to Au nanoparticle. In the meantime, concentrated electric field due to SPR of metal constituent can significantly enhance light absorption of CdS semiconductor and promote charge separation near the Au–CdS interface. Such synergetic effect enriches the electron (e-) on the Au tip for the efficient water reduction and leads to high efficient H_2 evolution activity. The bad H_2 evolution activity of the CdS/Au heterodimers mainly attributes

http://dx.doi.org/10.5772/61888

to the weak SPR and consequent visible light harvest of smaller sized Au (2–3 nm). On the other hand, in a concentric Au–CdS core–shell nanostructure with high structure symmetry, the electrons are retained in the Au core after photo excitation and charge separation and cannot participate in photocatalytic reaction; thus, the photon absorption of CdS is suppressed. As a result, almost no H_2 evolution is observed with concentric Au–CdS.

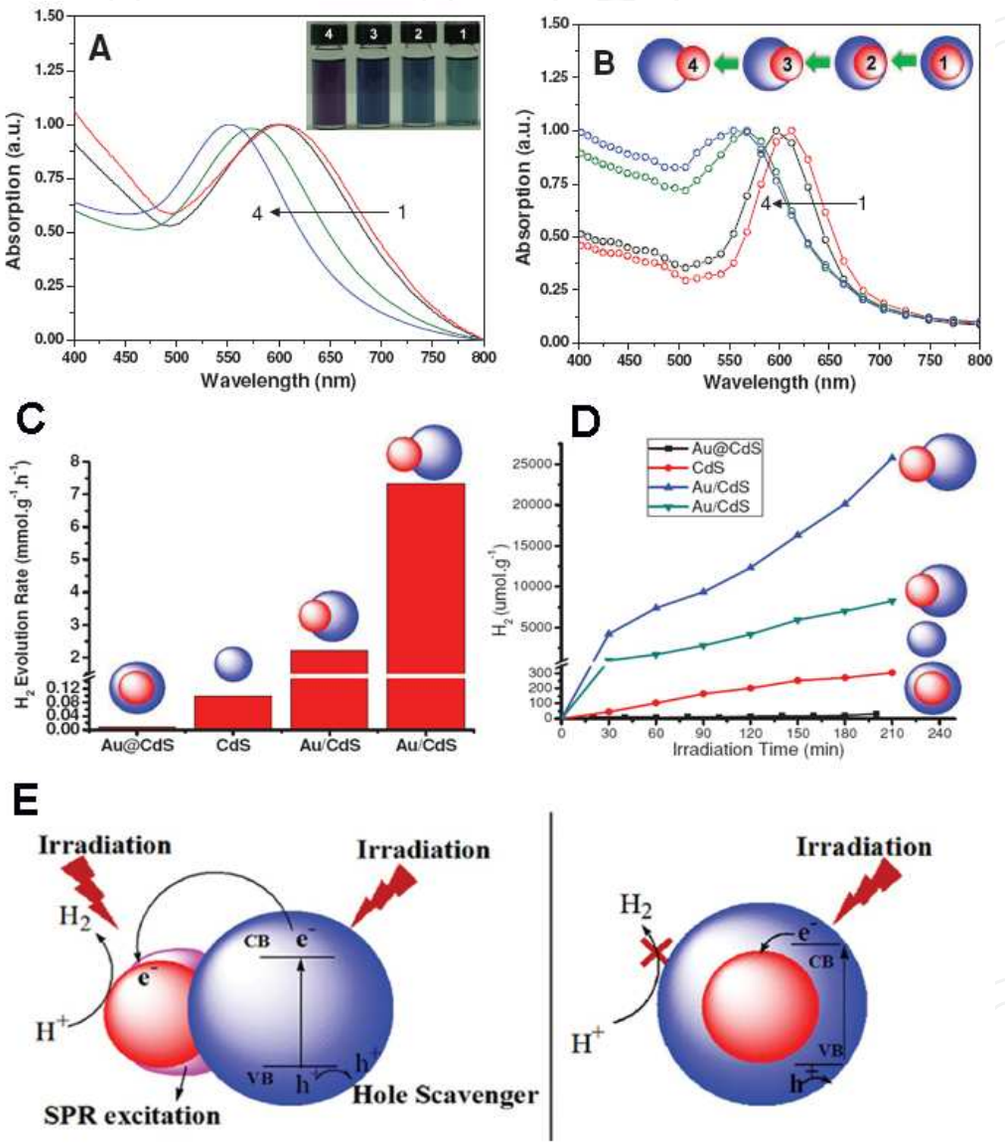

Figure 25. (A) Evolution of experimental UV-Vis absorption spectra with symmetry of Au/CdS colloid. (B) The normalized FDTD simulation of the SPR in these Au/CdS heteronanostructures. (C) Comparison of H_2 evolution activities of different Au–CdS photocatalysts. (D) Time evolution of photocatalytic generation of H_2 evolution amount versus irradiation time for them. (E) Schematic illustrations of visible light-induced electron/hole separation and transfer difference in heterodimer and core/shell Au/CdS when dispersed in aqueous solution containing sacrificial reagents. From Zhao et al. [32] with permission; copyright Wiley-VCH Verlag GmbH & Co. KGaA.

In conclusion, based on the series of metal-semiconductor hybrid nanostructures from concentric core–shell to nonconcentric heterodimer with precisely controlled separation

between metal and semiconductor constituents, the gradual symmetry evolution has led to novel control of optical response (plasmon–exciton coupling) and photocatalytic activity in hybrid nanostructures, which highlight the importance of nanoscale interface control for both fundamental understanding and technology applications. Thus, it can allow us to evaluate a possible upper limit of a photocatalytic reaction and guide the design toward high efficient hybrid nanostructures. Due to the plasmon intensity difference from different sized Au NPs, the larger sized Au, such as tens of nanometers to hundreds of nanometers size, the plasmon enhancement for photocatalysis may become strong.

4. The photoreduction of CO_2 applications of metal/semiconductor hybrid nanocrystals

Photoreduction of CO_2 is another important application of metal/semiconductor photocatalyst, and it directly converses CO_2 into organic compound such methane, methanol, formalin, formic acid, and so on [125–130]. Being similar with photocatalysis for hydrogen evolution, metal/semiconductor photocatalysts for photoreduction of CO_2 need some potential to meet the photocatalysis reaction (Schemes 1–5) [125],

$$H_2O \rightarrow H_2 + 1/2\ O_2, \Delta E = 1.23V \quad (1)$$

$$CO_2 + H_2O \rightarrow HCOOH + 1/2\ O_2, \Delta E = 1.40\ V \quad (2)$$

$$CO_2 + H_2O \rightarrow HCOH + O_2, \Delta E = 1.34\ V \quad (3)$$

$$CO_2 + H_2O \rightarrow\ CH_3OH + 3/2\ O_2, \Delta E = 1.21\ V \quad (4)$$

$$CO_2 + H_2O \rightarrow CH4 + 2\ O_2, \Delta E = 1.06\ V \quad (5)$$

and two pathways of photoreduction of CO_2: formalin pathway and carbine pathway are proposed to explain the mechanism of photoreduction of CO_2. According to these rules, various photocatalysts have been synthesized for conversing CO_2 into fuel and modified for higher conversion efficiency. What is needed to point out here is that the reduction potential of CO_2 depends on the reaction conditions, such as pH, and as the reduction is carried out, a series of reactions occur simultaneously. Therefore, as the reaction conditions vary, the main product of photoreduction of CO_2 is different.

http://dx.doi.org/10.5772/61888

Nowadays, several series of semiconductor have been used for photoreduction of CO_2, such as oxides [126, 131–133], sulfides [134], phosphide [135–136], and so on. In most case, metal will be used as cocatalysts to enhance photoreduction efficiency. Habisreutinger and his coworker have concluded photoreduction of CO_2 using semiconductors (Table 1) and in most of the cases, metal would be used as cocatalyst [132]. However, as using different metal as cocatalysts, the main products of photoreduction of CO_2 are different. It hints that metal nanocrystals play an important role in the photocatalysis system. It provides impossibility for tuning the photoreduction of CO_2 by doping metal cocatalysts.

As a kind of photocatalysts, TiO_2 is one of the most popular semiconductors for photoreduction of CO_2 [130]. For example, Li and her coworkers dope Cu onto TiO_2 nanocrystals supported with mesoporous silica and enhance the photoreduction of CO_2 (Figure 26A–D) [137]. More complex structure of photocatalysts has also been synthesized for photoreduction of CO_2. Wang and his coworkers prepared the CdSe/Pt/TiO_2 and monitor decrement of CO_2 under irradiation of visible light (wavelength > 420 nm). They found that TiO_2/Pt combining with CdSe platform a higher activity for photoreduction of CO_2 (Figure 26E and F) [133].

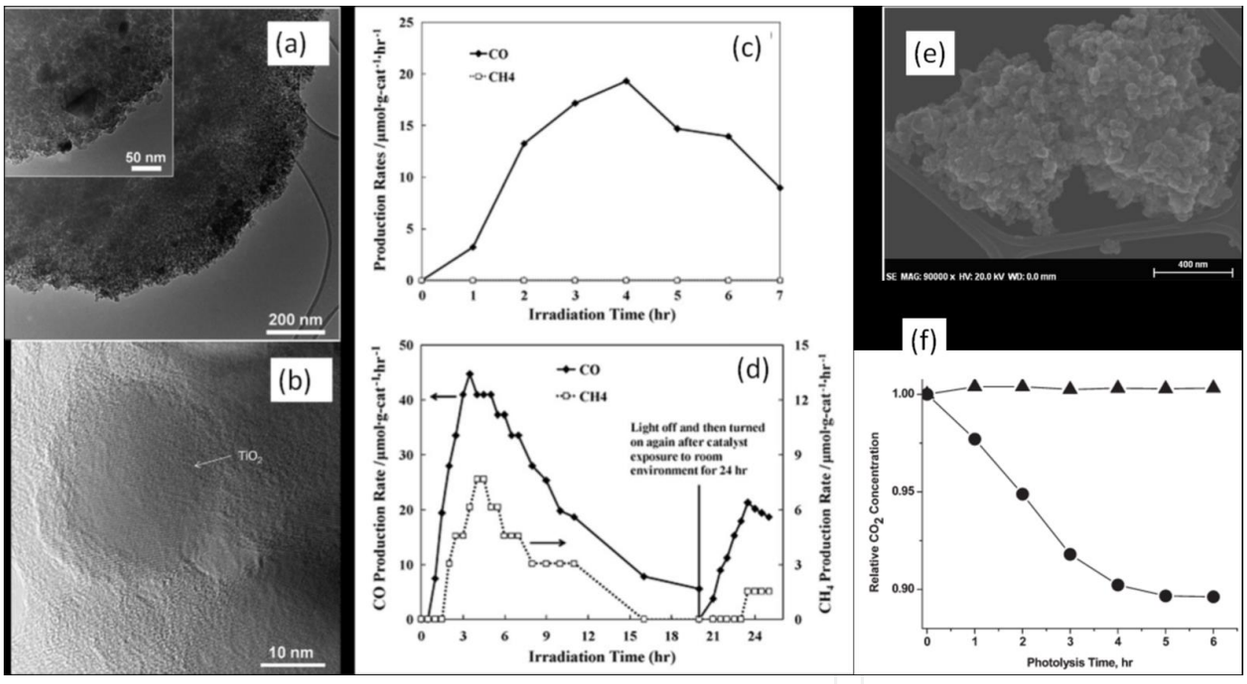

Figure 26. Cu/TiO_2 nanocrystals TEM (A) and HRTEM (B) images and its catalysis properties of photoreduction of CO_2 (C and D). Copyright: Elsevier, 2010. CdSe/Pt/TiO_2 nanocrystals and its photoreduction of CO_2 (E and F). Copyright: America Chemistry Society, 2010.

Beside TiO_2 nanocrystals photocatalyst, sulfides such as CdS nanocrystals and ZnS nanocrystals also show excellent properties for the photoreduction of CO_2. It is reported that using ZnS nanocrystals as photocatalyst, the rate of formic acid production is up to 7000 μmol h^{-1} g^{-1} [132, 134]. What's more, the shape of nanocrystals and other factors on photoreduction of CO_2 attract lots of attention and photoreduction of CO_2 (Figure 27) [138].

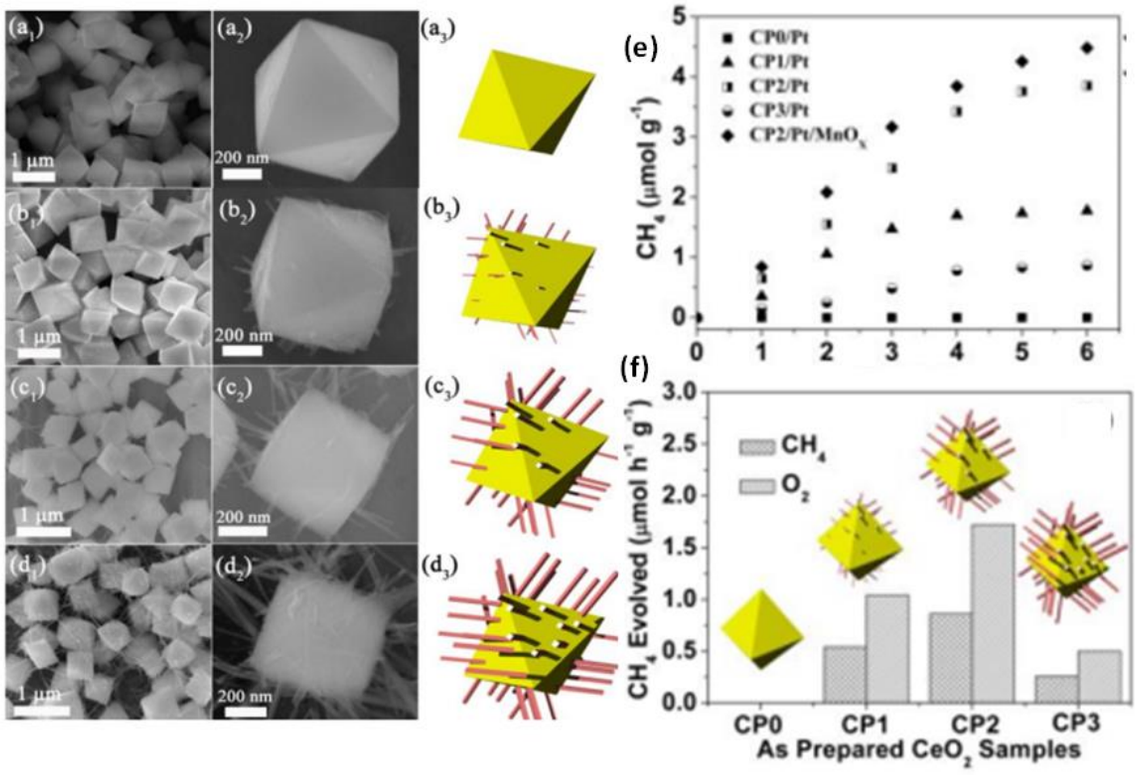

Figure 27. SEM images and schematic of CeO_2 modified with HPO_4 ions (A–D) and CH_4 evolution from photoreduction of CO_2 (E and F). Copyright: America Chemistry Society, 2015.

5. Some other recent photosynthesis applications of metal/semiconductor hybrid nanocrystals

Beside hydrogen evolution and photoreduction of CO_2 form photocatalysis, metal/semiconductor hybrid nanocrystals recently are used for photosynthesis applications. Metal or noble metal is usually employed as catalysts in organic synthesis [139]. Moreover, noble metal has plasmonic effect and induces the organic reaction under visible light and enhances the conversion efficiency [140]. Combining with semiconductor nanocrystals, metal/semiconductor hybrid nanocrystals have potential advantages in organic photosynthesis: higher conversion efficiency, higher selectivity, and lower by-products [141–143].

For instance, Au/CeO_2 is employed for oxidation of Alcohol forming aldehyde or ketone under irradiation of visible light [144]. The reaction rate depends on the surface area of Au nanoparticles, the power of irradiation and the function group of organic compound (Figure 28A–C), and a high selectivity of oxidation is also showed in such hybrid nanocrystals (Figure 28D–F). Beside, metal/semiconductor hybrid nanocrystals, such as Au/ZrO_2, can be used for other organic reaction: reduction of nitroaromatic compound, Suzuki reaction, ester reaction. and so on [140, 142–143].

http://dx.doi.org/10.5772/61888

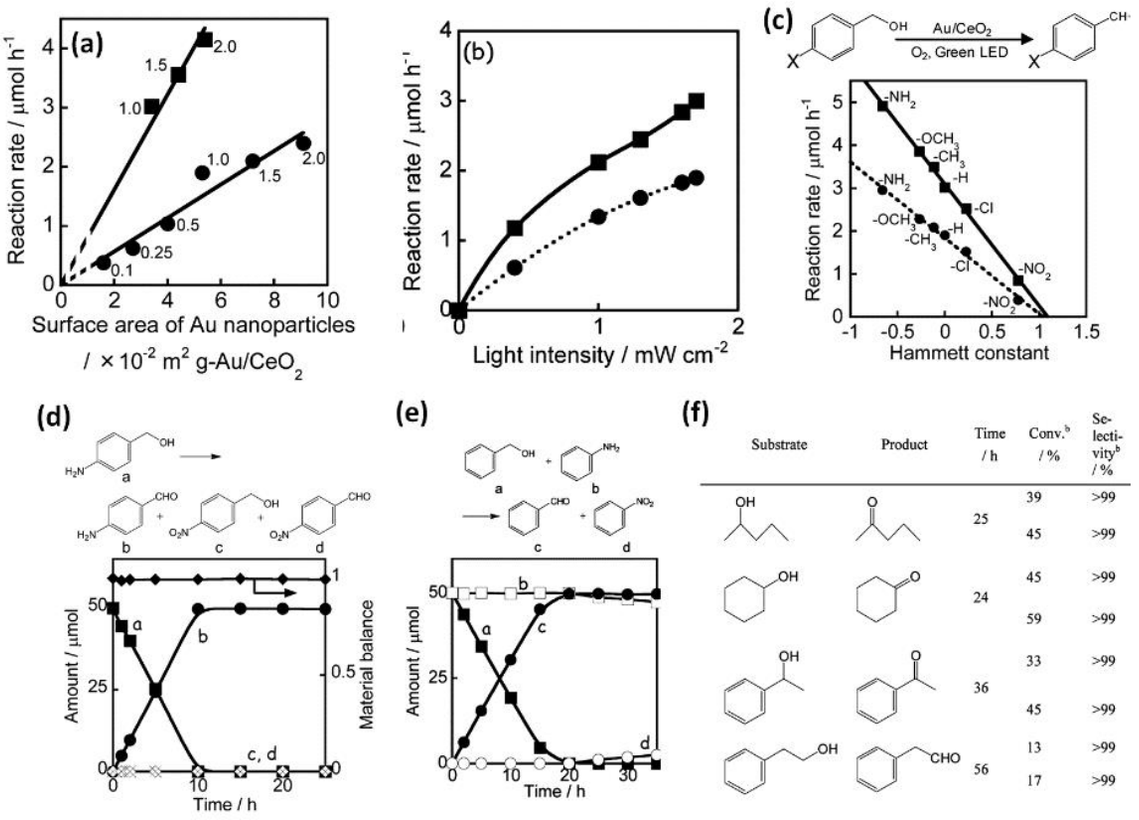

Figure 28. Reaction rate depending on surface area of Au nanoparticles (A), light intensity (B), and substituted functional groups. Copyright: America Chemistry Society, 2012.

In summary, metal/semiconductor photocatalysts have shown their potential application on hydrogen evolution, photoreduction for conversing CO_2 into fuel and organic photosynthesis. Although there is a long way before the metal/semiconductor hybrid nanocrystals being implemented in real-life application, more photocatalysts with different components, special architectures, or structures would be designed for the real-life application.

6. Summary and outlook

Metal/semiconductor hybrid NCs did have advantages on integration of functionalities of noble metal and semiconductors based on well-controlled morphologies and heterointerface control. Then they could have potential applications to improve the quantum yield of photoinduced electrons or holes for photoreduction and photooxidation. This review has demonstrated the recent research efforts to synthesize metal/semiconductor hybrid NCs and to understand and control the photocatalytic applications, such as photocatalytic water splitting, CO_2 photoreduction, and photoinduced organic synthesis. First, on the long term, it can be expected that innovative design and improved synthetic capabilities in the development of elaborate metal/semiconductor NCs with defined topologies and interface control will deliver exciting opportunities in both fundamental understanding and practical

exploitation of unconventional properties and functionalities stemming from properly engineered heterostructures with tailored interfaces and structural features. It can also be expected that some recent new synthesis strategy, such as the reaction between coordinated cation ions and semiconductor nanostructures (core/shell, heterodimers, doped NCs), nonepitaxial growth of metal/semiconductor core/shell, and heterodimers will speed up the precise photocatalysts synthesis and design. The new mechanism of photocatalysis, such as plasmon-enhanced photocatalysis, the synergistic cooperation of plasmonic metals, and cocatalysts based on well-defined interface will also boost each of them to an unprecedented level of catalytic performance.

Author details

Jiatao Zhang*, Muwei Ji, Jiajia Liu and Meng Xu

*Address all correspondence to: zhangjt@bit.edu.cn

Beijing Key lab of Construction Tailorable Advanced Functional Materials and Green Applications, School of materials and Engineering, Beijing Institute of Technology, Beijing, China

References

[1] Linic S., Christopher P., Ingram D. B.. Nat. Mater.. 2011; 10:911.

[2] Clavero C.. Nat. Photonics. 2014; 8:95.

[3] Zhang J. T., Tang Y., Lee K., Ouyang M.. Nature. 2010; 466:91.

[4] Jiang R. B., Li B. X., Fang C. H., Wang J. F.. Adv. Mater.. 2014; 26:5274.

[5] Yang J., Wang D., Han H., Li C.. Acc. Chem. Res.. 2013;46:1900.

[6] Xiao M., Jiang R., Wang F., Fang C., Wang J. F., Yu J. C.. J. Mater. Chem. A. 2013;1:5790.

[7] Warren S. C., Thimsen E.. Energy Environ. Sci.. 2012;5:5133.

[8] Ayers J. E. Heteroepitaxy of Semiconductors: Theory, Growth and Characterization. New York: CRC Press; 2007.

[9] Carbone L., Cozzoli P. D.. Nano Today. 2010;5:449.

[10] Casavola M., Buonsanti R., Caputo G., Cozzoli P. D.. Eur. J. Inorg. Chem.. 2008;6:837.

[11] Lee J., Hernandez P., Lee J., Govorov A. O., Kotov N. A.. Nat. Mater.. 2007;4:291.

[12] Gao J. H., Gu H. W., Xu B. Chem. Res.. 2009;42:1097.

[13] Costi R., Saunders A. E., Banin U. Angew. Chem. Int. Ed.. 2010;49:4878.

[14] Wang C., Xu C., Zeng H., Sun S. Adv. Mater.. 2009;21:3045.

[15] Jin Y. D., Gao X. H. Nat. Nanotechnol.. 2004;4:571.

[16] Yang J., Sargent E. H., Kelley S. O., Ying J. Y. Nat. Mater.. 2009;8:683.

[17] Yang J., Ying J. Y. J. Am. Chem. Soc.. 2010;132:2114.

[18] Buck M. R., Bondi J. F., Schaak R. E. Nat. Chem.. 2012;4:37.

[19] Atwater H. A., Polman A. Nat. Mater.. 2010;9:205.

[20] Gu H., Zheng R., Zhang X., Xu B. J. Am. Chem. Soc.. 2004;126:5664.

[21] Wang C., Yin H., Dai S., Sun S.H. Chem. Mater.. 2010;22:3277.

[22] Wu H., Chen O., Zhuang J., Lynch J., Montagne D. L., Nagaoka Y., Cao Y. C. J. Am. Chem. Soc.. 2011;133:14327.

[23] Figuerola A., Fiore A., Corato R. D., Falqui A., Giannini C., Micotti E., Lascialfari A., Corti M., Cingolani R., Pellegrino T., Cozzoli P. D., Manna L. J. Am. Chem. Soc.. 2008;130:1477.

[24] Cozzoli P. D., Pellegrino T., Manna L. Chem. Soc. Rev.. 2006;35:1195.

[25] Mokari T., Rothenberg E., Popov I., Costi R., Banin U. Science. 2004;304:1787.

[26] Costi R., Saunders A. E., Elmalem E., Salant A., Banin U. Nano Lett.. 2008;8:637.

[27] Du Y., Chen B., Yin Z., Liu Z., Zhang H. Small. 2014;10:4727.

[28] Zhang J. T., Tang Y., Lee K., Ouyang M. Science. 2010;327:1634.

[29] Zhang J., Tang Y., Weng L., Ouyang M. Nano lett.. 2009;9:4061.

[30] Anson C. E., Eichhöfer A., Issac I., Fenske D., Fuhr O., Sevillano P., Persau C., Stalke D., Zhang J. Angew. Chem. Int. Ed.. 2008;47:1326.

[31] Gui J., Ji M., Liu J., Xu M., Zhang J. T., Zhu H. S. Angew. Chem. Int.. 2015;54:1.

[32] Zhao Q., Ji M., Qian H., Dai B., Weng L., Gui J., Zhang J. T., Ouyang M., Zhu H. S. Adv. Mater.. 2014;26:1387.

[33] Qian H., Zhao Q., Dai B., Guo L., Zhang J., Liu J., Zhang J. T., Zhu H. S. NPG Asia Mater.. 2015;7:e152.

[34] Son D. H., Hughes S. M., Yin Y., Alivisatos A. P., Science. 2004; 306:1009.

[35] Jeong U. Y., Xia Y. N., Yin Y. D.. Chem. Phys. Lett.. 2005;416:246.

[36] Ryzhii M., Ryzhii V. Physics and Modeling of Tera- and Nano-Devices. In: World Scientific; 2008; Singapore.

[37] McBride J., Treadway J., Feldman L. C., Pennycook S. J., Rosenthal S. J. Nano Lett.. 2006;6:1496.

[38] Battaglia D., Li J. J., Wang Y., Peng X. Angew. Chem. Int. Ed.. 2003;42:5035.

[39] Kim S., Fisher B., Eisler H. J., Bawendi M. J. Am. Chem. Soc.. 2003;125:11466.

[40] Smith A. M., Nie S. Acc. Chem. Res.. 2010;43:190.

[41] Klimov V. I., Ivanov S. A., Nanda J., Achermann M., Bezel I., McGuire J. A., Piryatinski A.. Nature. 2007;441:447.

[42] Caruge J. M., Halpert J. E., Wood V., Bulovic V., Bawendi M. G. Nat. Photonics. 2008;2:247.

[43] Sargent E. H. Nat. Photonics. 2009;3:325.

[44] Chen X. B., Lou Y., Samia A. C., Burda C. Nano Lett.. 2003;3:799.

[45] Peng X. G., Schlamp M. C., Kadavanich A. V., Alivisatos A. P.. J. Am. Chem. Soc.. 1997;119:7019.

[46] Wang Z. L.. J. Phys. Chem. B.. 2000;104:1152.

[47] Palmstrøm C. J.. Annu. Rev. Mater. Sci.. 1995;25:389.

[48] Lee J. S., Shevchenko E. V., Talapin D. V.. J. Am. Chem. Soc.. 2008;130:9673.

[49] Kim H., Achermann M., Balet L. P., Hollingsworth J. A., Klimov V. I.. J. Am. Chem. Soc.. 2005;127:544.

[50] Mokari T., Sztrum C. G., Salant A., Rabani E., Banin U.. Nat. Mater.. 2005;4:855.

[51] Mokari T., Rothenberg E., Popov I., Costi R., Banin U.. Science. 2004;304:1787.

[52] Wang C., Xu C., Zeng H., Sun S.. Adv. Mater.. 2009;21:3045.

[53] Fang C., Jia H., Chang S., Ruan Q., Wang P., Chen T., Wang J.. Energy Environ. Sci.. 2014;7:3431.

[54] Sun Z., Yang Z., Zhou J., Yeung M., Ni W., Wu H., Wang J.. Angew. Chem. Int. Ed.. 2009;48:2881.

[55] Lambright S., Butaeva E., Razgoniaeva N., Hopkins T., Smith B., Perera D., Corbin J., Khon E., Thomas R., Moroz P., Mereshchenko A., Tarnovsky A., Zamkov M. ACS Nano. 2014;8:352.

[56] Priebe M., Fromm K. M.. Chemistry—A European Journal. 2015;21:3854.

[57] Güttel R., Paul M.,Schüth F.. Catal. Sci. Technol.. 2011;1:65.

[58] Li A., Zhang P., Chang X., Cai W., Wang T., Gong J.. Small. 2015;11:1892.

[59] Li G., Tang Z.. Nanoscale. 2014;6:3995.

[60] Fang Q., Xuan S., Jiang W., Gong X.. Adv. Funct. Mater.. 2011;21:1902.

[61] Jun Z., Ling X., Jiali S., Diping H., Huan. J. Surf. Coat. Technol.. 2015;271:119.

[62] Zhang Q., Lee I., Joo J. B., Zaera F., Yin Y.. Acc. Chem. Res.. 2013;46:1816.

[63] Zhao L., Peng J., Huang Q., Li C., Chen M., Sun Y., Lin Q., Zhu L., Li F.. Adv. Funct. Mater.. 2014;24:363.

[64] Zhang N., Fu X., Xu Y.J.. J. Mater. Chem.. 2011;21:8152.

[65] Zhang L., Blom D. A., Wang H.. Chem. Mater.. 2011;23:4587.

[66] Park J. C., Lee H. J., Jung H. S., Kim M., Kim H. J., Park K. H., Song H.. ChemCatChem. 2011;3:755.

[67] Hah H. J., Um J. I., Han S. H., Koo S. M.. Chem. Commun.. 2004;:1012.

[68] Tan L., Chen D., Liu H., Tang F.. Adv. Mater.. 2010;22:4885.

[69] Fan C. M., Zhang L. F., Wang S. S., Wang D. H., Lu L. Q., Xu A. W.. Nanoscale. 2012;4:6835.

[70] Gröger H., Gyger F., Leidinger P., Zurmühl C., Feldmann C.. Adv. Mater.. 2009;21:1586.

[71] Lin Y. S., Wu S. H., Tseng C. T., Hung Y., Chang C., Mou C. Y.. Chem. Commun.. 2009;:3542.

[72] Priebe M., Fromm K. M.. Part. Part. Syst. Charact.. 2014;31:645.

[73] Park J. C., Heo E., Kim A., Kim M., Park K. H., Song H.. J. Phys. Chem. C. 2011;115:15772.

[74] Arnal P. M., Comotti M., Schuth F.. Angew. Chem. Int. Ed.. 2006;45:8224.

[75] Lou X. W., Yuan C., Archer L. A.. Small. 2007;3:261.

[76] Guan B., Wang T., Zeng S., Wang X., An D., Wang D., Cao Y., Ma D., Liu Y., Huo Q.. Nano Res.. 2014;7:246.

[77] Yeo K. M., Shin J., Lee I. S.. Chem. Commun.. 2010;46:64.

[78] Wang M., Han J., Xiong H., Guo R.. Langmuir. 2015;31:6220.

[79] Fujishima A., Honda K.. Nature. 1972;238:37.

[80] Kudo A., Miseki Y.. Chem. Soc. Rev.. 2009;38:253.

[81] Linsebigler A. L., Lu G., Yates J. T.. Chem. Rev.. 1995;95:735.

[82] Li X., Yu J., Low J., Fang Y., Xiao J., Chen X.. J. Mater. Chem. A. 2015;3:2485.

[83] Osterloh F. E.. Chem. Soc. Rev.. 2013;42:2294.

[84] Maeda K.. J. Photoch. Photobio. C. 2011;12:237.

[85] Qu Y., Duan X. F.. Chem. Soc. Rev.. 2013;42:2568.

[86] Chen X., Shen S., Guo L., Mao S. S.. Chem. Rev.. 2010;110:6503.

[87] Ma Y., Wang X., Jia Y., Chen X., Han H., Li C.. Chem. Rev.. 2014;114:9987.

[88] Kraeutler B., Bard A. J.. J. Am. Chem. Soc.. 1978;100:4317.

[89] Yang J., Wang D., Han H., Li C.. Acc. Chem. Res.. 2013;46:1900.

[90] Wang H., Zhang L., Chen Z.G., Hu J., Li S., Wang Z., Liu J., Wang X. Chem. Soc. Rev.. 2014;43:5234.

[91] Bai S., Jiang J., Zhang Q., Xiong Y. J. Chem. Soc. Rev.. 2015;44:2893.

[92] Jing L., Zhou W., Tian G., Fu H. G. Chem. Soc. Rev.. 2013;42:9509.

[93] Kochuveedu S. T., Jang Y. H., Kim D. H. Chem. Soc. Rev.. 2013;42:8467.

[94] Ran J., Zhang J., Yu J., Jaroniec M., Qiao S. Z. Chem. Soc. Rev.. 2014;43:7787.

[95] Thanminimulla C. T. K., Takata T., Hara M., Kondo J. N., Domen K. J. Catal.. 2000;196:362.

[96] Yamada Y., Miyahigashi T., Kotani H., Ohkubo K., Fukuzumi S. Energy Environ. Sci.. 2012;5:6111.

[97] Awazu K., Fujimaki M., Rockstuhl C., Tomingaga J., Murakami H., Ohiki Y., Yoshida N., Watanabe T. J. Am. Chem. Soc.. 2008;130:1676.

[98] Chen X., Zhu H., Zhao J., Zheng Z., Gao X. Angew. Chem. Int. Ed.. 2008;47:5353.

[99] Wang P., Huang B., Qin X., Zhang X., Dai Y., Wei J., Wang M. H. Angew. Chem. Int. Ed.. 2008;47:7931.

[100] SWalclawik., E. R., Zhu H. Green Chem.. 2013;15:1814.

[101] Lang X., Chen X., Zhao J. Chem. Soc. Rev.. 2014;43:473.

[102] Jones M. R., Osberg K. D., Macfarlane R. J., Langille M.R., Mirkin C. A. Chem. Rev.. 2011;111:3736.

[103] Jiang R., Li B., Fang C., Wang J. F. Adv. Mater.. 2014;26:5274.

[104] Kochuveedu S. T., Jang Y. H., Kim D. H. Chem. Soc. Rev.. 2013;42:8467.

[105] Ingram D. B., Linic S. J. Am. Chem. Soc.. 2011;133:5202.

[106] Pu Y., Wang G., Chang K., Ling Y., Lin Y., Fitzmorris B. C., Liu C., Lu X., Tong Y., Zhang J. Z., Hsu Y., Li Y. Nano Lett.. 2013;13:3817.

[107] Seh Z. W., Liu S., Low M., Zhang S., Liu Z., Mlayah A., Han M. Y. Adv. Mater.. 2012;24:2310.

[108] Pradhan S., Ghosh D., Chen S. ACS Appl. Mater. Interfaces. 2009;1:2060.

[109] Zhang Z., Zhang L., Hedhili M. N., Zhang H., Wang P. Nano Lett.. 2013;13:14.

[110] Qian K., Sweeny B. C., Johnston-Peck A. C., Niu W., Graham J. O., Duchenen J. S., Qiu J., Wang Y., Engelhard M. H., Su D., Stach E. A., Wei W. D. J. Am. Chem. Soc.. 2014;136:9842.

[111] Long R., Mao K. K., Gong M., Zhou S., Hu J. H., Zhi M., You Y., Bai S., Jiang J., Zhang Q., Wu X. J., Xiong Y. J.. Angew. Chem. Int. Ed.. 2014;53:3205.

[112] Liu G., Yang H. G., Pan J., Yang Y. Q., Lu G. Q., Cheng H. M. Chem. Rev.. 2014;114:9559.

[113] Ohno T., Sarukawa K., Matsumura M.. New J. Chem.. 2002;26:1167.

[114] Yang H. G., Sun C. H., Qiao S. Z., Zou J., Liu G., Smith S.C., Cheng H. M., Lu G. Q.. Nature. 2008;453:638.

[115] Murakami N., Kurihara Y., Tsubota T., Ohno T.. J. Phys. Chem. C. 2009;113:3062.

[116] Liu C., Han, X.; Xie, S.; Kuang, Q.; Wang, X.; Jin, M.; Xie, Z.; Zheng, L.. Chem. Asian J.. 2013;8:282.

[117] Tian Y., Tasuma T. J. Am. Chem. Soc.. 2005;127:7632.

[118] Silva C. G., Juárez R., Marino T., Molinari R., García H. J. Am. Chem. Soc.. 2011;133:595.

[119] Kelly K. L., Coronado E., Zhao L. L., Schatz G. C. J. Phys. Chem. B.. 2003;107:668.

[120] Maeda K., Domen K. J. Phys. Chem. C. 2007;111:7851.

[121] Hu P., Pramana S. S., Cao S., Ngaw C. K., Lin J. D., Loo S. C. J., Tan T. T. Y. Adv. Mater.. 2013;25:2567.

[122] Cao S. W., Fang J., Shahjamali M. M., Boey F. Y. C., Barber J., Loo S. C. J., Xue C. RSC Adv.. 2012;2:5513.

[123] Yan H., Yang J. H., Ma G. J., Wu G. P., Zong X., Lei Z. B., Shi J., Li C. J. Catal.. 2009;266:165.

[124] Yang J., Yan H., Wang X., Wen F., Wang Z., Fan D., Shi J., Li C. J. Catal.. 2012;290:151.

[125] Liu C., Dasgupta N. P., Yang, P.. Chem. Mater.. 2014;26:415.

[126] Schneider J., Matsuoka M., Takeuchi M., Zhang J., Horiuchi Y., Anpo M., Bahnemann D. W.. Chem. Rev.. 2014;114:9919.

[127] Ma Y., Wang X., Jia Y., Chen X., Han H., Li C.. Chem. Rev.. 2014;114:9987.

[128] Kubacka A., Fernández-García M., Colón, G.. Chem. Rev.. 2012;112:1555.

[129] Wen F., Li, C.. Acc. Chem.Res.. 2013;46:2355.

[130] Cokoja M., Bruckmeier C., Rieger B., Herrmann W. A., Kühn F. E.,. Angew. Chem. Int. Ed.. 2011;50:8510.

[131] Kang Q., Wang T., Li P.; Liu L.; Chang K.; Li M.; Ye J.. Angew. Chem. Int. Ed.. 2015;54:841.

[132] Habisreutinger S. N.; Schmidt-Mende L.; Stolarczyk J. K.. Angew. Chem. Int. Ed.. 2013;52:7372.

[133] Wang C.; Thompson R. L.; Baltrus J.; Matranga C.. J. Phy. Chem. Lett.. 2010;1:48.

[134] Johne P., Kisch H.. J. Photochem. Photobiol. A. 1997;111:223.

[135] Inoue T., Fujishima A., Konishi S., Honda, K.. Nature. 1979;277:637.

[136] Sato S., Arai T., Morikawa T., Uemura K., Suzuki T. M., Tanaka H., Kajino, T.. J. Am. Chem. Soc.. 2011;133:15240.

[137] Li Y., Wang W.N., Zhan Z., Woo M.H., Wu C.Y., Biswas P.. Appl. Catal. B. Environ.. 2010;100:386.

[138] Li P., Zhou Y., Zhao Z., Xu Q., Wang X., Xiao M., Zou Z.. J. Am. Chem. Soc.. 2015;137:9547.

[139] Wu Y., Wang D., Zhao P., Niu Z., Peng Q., Li Y.. Inorg. Chem.. 2011;50:2046.

[140] Wang F., Li C., Chen H., Jiang R., Sun L. D., Li Q., Wang J., Yu J. C., Yan C. H.. J. Am. Chem. Soc.. 2013;135:5588.

[141] Kisch H.. Angew. Chem. Int. Ed.. 2013;52:812.

[142] Xiao Q., Liu Z., Bo A., Zavahir S. Sarina S., Bottle S., Riches J. D., Zhu H.. J. Am. Chem. Soc.. 2015;137:1956.

[143] Zhu H., Ke X., Yang X., Sarina S., Li, H.. Angew. Chem. Int. Ed.. 2010;49:9657.

[144] Tanak, A., Hashimot, K., Kominam, H.. J. Am. Chem. Soc.. 2012;134:14526.